Ben-Gurion University of the Negev

The Faculty of Natural Sciences

The Department of Physics

Point Source Atom Interferometry for Rotation Sensing

Thesis submitted in partial fulfillment of the requirements for the Master of Sciences degree (M.Sc)

By

Yali Cina

The research work for the thesis has been carried out under the supervision of

Prof. Ron Folman

November 2024

Point Source Atom Interferometry for Rotation Sensing

Yali Cina

Master of Sciences Thesis

Ben-Gurion University of the Negev

2024

Abstract

This thesis presents the development of a Point Source Atom Interferometer (PSI) for high-precision rotation sensing. We explore both experimental and theoretical advancements in PSI technology, with a focus on enhancing sensitivity, dynamic range, and potential for miniaturization.

Our experimental work involves the design and construction of a versatile dual-chamber apparatus, comprising a two-dimensional magneto-optical trap (2D-MOT) for cold atom generation and a three-dimensional MOT (3D-MOT) chamber for atom trapping and interferometry. A key ingredient is the integration of high-gradient magnetic coils within the vacuum chamber, enabling strong atom confinement while minimizing power consumption and heat generation.

On the theoretical front, we introduce the Squeezed Point Source Interferometer (SPSI) method, which incorporates a repulsive potential to manipulate the atomic ensemble's phase-space distribution prior to the interferometer sequence. Through analytical derivations and numerical simulations, we demonstrate that SPSI can enhance the interferometer's sensitivity by up to two orders of magnitude while simultaneously reducing the cycle time.

We present a comprehensive performance analysis, introducing a compactness factor that encapsulates sensitivity, dynamic range, and device size. Our results show improvements of up to four orders of magnitude over standard PSI configurations, paving the way for the development of chip-scale atom interferometers for rotation sensing.

This work contributes to the advancement of atom interferometry technology, pushing the boundaries of precision measurement while making significant progress toward practical, compact devices for real-world applications in inertial navigation, geophysics, and fundamental physics tests.

Publications

"Chip-Scale Point-Source Sagnac Interferometer by Phase-Space Squeezing", Y. Halevy, Y. Cina, O. Feldman, D. Groswasser, Y. Japha, and R. Folman, arXiv:2405.16972 (2024).

"A Method for Miniaturizing a Rotation Sensor based on Cold Atoms", Y. Halevy, Y. Cina, O. Feldman, D. Groswasser, Y. Japha, and R. Folman, patent application no. 312257 (2024).

Acknowledgements

I would like to thank all those who participated in this thesis project and stood by my side throughout. This project represents the culmination of a significant period in my life and education, during which I was a member of Prof. Ron Folman's Atom Chip group.

First, I thank my advisor, Prof. Ron Folman, for this work and the opportunity to be part of a research project. Throughout my time under his guidance, he consistently gave me the freedom to approach my work independently, allowing me to learn and overcome challenges along the way. He also provided invaluable guidance from his extensive experience and knowledge - and not only in the field of physics.

Secondly, I want to thank my lab partner of the past two years, Yiftach Halevy. We conducted most of the work presented in this thesis together, through many hours in the lab and daily communication. I appreciate your desire to understand everything thoroughly, which drove me to do the same. I had a great time working with you and learned a lot about small team dynamics.

I also need to mention Omer Feldman, with whom I worked in the initial stages of this project. We both started with almost no background and had to help each other understand the physics and manage the various systems in the lab. I truly enjoyed working with you and learned much from our time together.

I am deeply grateful to two additional mentors who played crucial roles in my research journey. Dr. David Grosswasser's expertise in experimental techniques was invaluable to my laboratory work. David, your vast experience and knowledge were instrumental in every aspect of my practical research. Under your guidance, I not only expanded my understanding of physics but also gained invaluable insights into the nuances of laboratory operations. Our collaborative work, your mentorship, and our engaging discussions about physics were highlights of my research experience. Equally significant was Dr. Yonathan Japha's contribution to the theoretical aspects of my work. Yoni, your unique approach to theoretical physics opened new perspectives for me. I learned immensely from observing how you tackle complex physical problems. Your consistent willingness to address my queries, no matter how frequent or fundamental, was extraordinary and deeply appreciated. Both of you have profoundly shaped my development as a researcher, and for that, I am truly thankful.

Another person who played an important role during my time in the group is Dr. Menachem Givon. You introduced me to the field of quantum technology as my primary mentor in the early stages in the lab. Whether technical knowledge or theoretical understanding of the systems, you always provided thorough answers and guidance.

I want to thank my neighbors at the optical table, Yosef and Yotam. For the past two years, we have shared the same lab, and you were always there for any question or when I needed help. I also want to thank all of the other students in our group who were happy to discuss difficult problems or help troubleshoot issues in the system.

The success of any laboratory hinges on the dedication of its support staff, and in this regard, I owe a great debt of gratitude to Yaniv, Zina, Sergey, and Sela. Your contributions were far more than just technical; they were the bedrock upon which our research stood. It is no overstatement to say that without your tireless efforts, our experiments would have ground to a halt. Your readiness to assist, often

at a moment's notice, was truly remarkable. Your spirit of collaboration and camaraderie created an environment where scientific inquiry could flourish.

Finally, I wish to express my heartfelt gratitude to those who provided unwavering support from outside the academic sphere. My deepest thanks go to Klil, my life partner, who patiently endured my endless discussions about quantum physics, lasers, and other esoteric subjects far removed from her own expertise. Her understanding and support have been invaluable. I am equally grateful to my parents and family, whose genuine interest in my work and constant encouragement have been a source of motivation throughout this journey. I also want to acknowledge my friends, both from my university days and before, who have been there to offer encouragement, lend an ear, or simply provide a much-needed distraction when the pressures of research mounted. Your collective support has been a crucial pillar in my academic journey, reminding me of the world beyond the laboratory and helping me maintain balance in my pursuits.

Contents

List of Figures

1 Introduction

Atom interferometry has emerged as a powerful technique for high-precision measurements in fundamental physics and applied sensing. By exploiting the wave nature of matter, atom interferometers can achieve exquisite sensitivity to inertial effects, gravitational fields, and fundamental constants. The field originated with pioneering experiments in 1991 demonstrating interference with neutral atoms [1–5], and has since grown rapidly, with an acceleration of research efforts in the last decade.

The principle of atom interferometry relies on the manipulation of atomic wave packets using laser pulses to create quantum superpositions and interference. Cold atom sources are typically used to enhance coherence time and precision. A key advantage of atom interferometers over their optical counterparts is the much larger effective energy associated with massive particles than with photons, potentially leading to greatly enhanced sensitivity [6–8].

Atom interferometers have a wide range of applications, including inertial guidance [9, 10], geophysics [11] and space-based research [12–15]. These often rely on two-photon Raman transitions for manipulating atomic wave packets, which have become a standard technique in the field [16–22].

Recent research has focused on several key areas to improve the performance of atom interferometers. Efforts have been directed towards increasing the interrogation time and physical size of the interferometer to enhance sensitivity, as demonstrated in experiments with long-baseline and fountain configurations [23, 24]. Researchers have also been developing large momentum transfer techniques to increase the interferometer area, including the use of Bloch oscillations and multi-photon Bragg diffraction [25–37]. The utilization of quantum resources such as squeezed states to surpass the standard quantum limit has been explored [38, 39], offering potential improvements in measurement precision.

In parallel, there has been significant work on engineering compact and portable systems suitable for field use [40–42], addressing the challenges of taking atom interferometers out of the laboratory. This includes efforts to miniaturize components and develop robust laser systems. These advancements collectively aim to push the boundaries of atom interferometry, enabling new applications in fundamental physics tests, geodesy, and inertial navigation. By addressing key challenges in sensitivity, portability, and practical implementation, researchers are working towards realizing the full potential of atom interferometry for high-precision inertial measurements.

This thesis focuses on the development and optimization of a Point Source Atom Interferometer (PSI) for rotation sensing. The PSI technique, first demonstrated by Dickerson et al. [43], utilizes a single expanding cloud of cold atoms to measure rotation rates by analyzing the spatial frequency of atomic density fringes. This approach offers several advantages over traditional atom interferometers, including simplified experimental configurations and multi-axis sensing capabilities.

Our work encompasses both experimental and theoretical advances in PSI technology. On the experimental front, we have designed and constructed a versatile apparatus comprising a two-dimensional magneto-optical trap (2D-MOT) for cold atom generation and a three-dimensional MOT (3D-MOT) chamber that serves as both the atom trap and interferometry region. This dual-chamber design, detailed in Sec. 4, allows for efficient production and manipulation of cold ^{87}Rb atoms. A key feature of

our setup is the integration of high-gradient magnetic coils within the vacuum chamber, enabling strong atom confinement while minimizing power consumption and heat generation.

The laser systems, crucial for atom cooling, trapping, and coherent manipulation, are described in Sec. 4.2. We employ a combination of distributed Bragg reflector (DBR) lasers for the MOT operations and a narrow-linewidth telecom laser system for Raman transitions. Careful design of the optical paths and precise control of laser frequencies and powers are essential for achieving the desired atomic state preparation and interferometric sequences.

A significant portion of this thesis is dedicated to the theoretical development and numerical simulation of an enhanced PSI technique, which we term the Squeezed Point Source Interferometer (SPSI). As presented in Sec. 5, the SPSI method incorporates a repulsive potential to manipulate the phase-space distribution of the atomic ensemble prior to the interferometer sequence. This novel approach, analyzed through both analytical derivations and numerical simulations, demonstrates substantial improvements in sensitivity, dynamic range and potential for miniaturization, compared to conventional PSI techniques.

Our performance analysis, detailed in Sec. 5.3, reveals that the SPSI method can enhance the interferometer sensitivity by up to two orders of magnitude while simultaneously reducing the cycle time. Moreover, we introduce a compactness factor that encapsulates sensitivity, dynamic range, and device size, demonstrating improvements of up to four orders of magnitude over standard PSI configurations. These advancements open the door to the development of chip-scale atom interferometers for rotation sensing, with potential applications in inertial navigation, geophysics, and tests of fundamental physics.

The thesis is structured as follows: Sec. 2 provides the theoretical foundations of atom interferometry, coherent manipulation techniques, and the PSI method. Sec. 3 discusses various noise sources affecting atom interferometers and presents our strategies for noise mitigation. The experimental apparatus is described in detail in Sec. 4. Sec. 5 introduces the SPSI concept, including analytical derivations, numerical simulations, and performance analysis.

On the basis of this work, we aim to contribute to the advancement of atom interferometry technology, pushing the boundaries of precision measurement while making strides towards practical, compact devices for real-world applications.

2 Theory

This section aims to provide a comprehensive overview of the key concepts and principles underlying atom interferometry, particularly focusing on its application to rotation sensing. We begin by examining the fundamental interactions between light and matter (Sec. 2.1), which form the basis for coherent manipulation of atomic states. We then explore the mechanics of two-photon Raman transitions (Sec. 2.2), a crucial technique for state manipulation in atom interferometry. Following this stage, we explore the principles of Mach-Zehnder atom interferometry (Sec. 2.3), a widely used configuration for precision measurements. Finally, we introduce the Point Source Interferometer (PSI, Sec. 2.4), an interferometer technique that offers unique advantages in rotation sensing and forms the core of our research. Throughout this section, we will bridge the gap between semi-classical descriptions and fully quantum mechanical treatments, providing insight into both the practical implementation and fundamental limits of atom interferometric rotation sensors.

2.1 Light-Matter Coherent Manipulation

The interaction between light and matter at the quantum level forms the foundation for many modern atomic physics experiments and quantum technologies. In this section, we explore the theoretical framework underlying the coherent manipulation of atomic two-state systems using electromagnetic radiation.

2.1.1 Two-Level Quantum System

The state of a two-level quantum system, such as specific hyperfine levels in alkali atoms, can be represented as a superposition of two eigenstates of the unperturbed Hamiltonian H_0:

$$|\Psi\rangle = C_0|0\rangle + C_1|1\rangle, \tag{1}$$

where C_0 and C_1 are complex probability amplitudes satisfying $|C_0|^2 + |C_1|^2 = 1$.

The state of a two-level system can be geometrically visualized on the Bloch sphere (Fig. 1). In this representation, any pure state of the system corresponds to a point on the surface of a unit sphere in three-dimensional space. The north and south poles of the sphere represent the basis states $|0\rangle$ and $|1\rangle$ respectively, while any other point on the sphere's surface corresponds to a superposition state. The state $|\Psi\rangle$, from Eq. 1, can be parameterized using spherical coordinates θ and ϕ:

$$|\Psi\rangle = \cos\frac{\theta}{2}|0\rangle + e^{i\phi}\sin\frac{\theta}{2}|1\rangle. \tag{2}$$

The Bloch vector $\vec{v_b}$ is defined as:

$$\vec{v_b} = \begin{pmatrix} \sin\theta\cos\phi \\ \sin\theta\sin\phi \\ \cos\theta \end{pmatrix}. \tag{3}$$

This vector provides a convenient way to visualize and manipulate the quantum state.

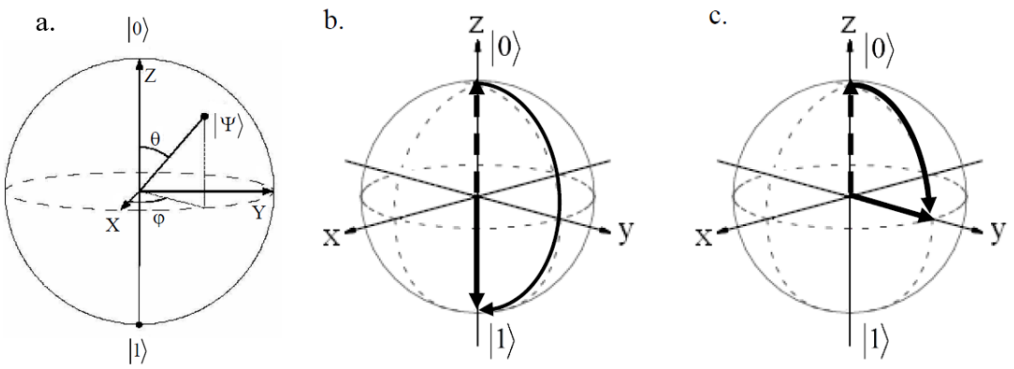

Figure 1: Bloch sphere [44]: (a) A general representation of a Bloch vector for a two-level system. (b) and (c) are examples of Rabi pulses, where the dashed line is the Bloch vector before the pulse, and the full line is the vector after the pulse. These examples refer to the π pulse (b) and $\pi/2$ pulse (c).

2.1.2 Rabi Oscillations

When subjected to coherent radiation, the evolution of the system can be described by the time-dependent Schrödinger equation:

$$i\hbar\frac{\partial|\Psi\rangle}{\partial t} = (H_0 + V(t))|\Psi\rangle, \tag{4}$$

where $V(t)$ represents the atom-light interaction. In the rotating wave approximation, this leads to the phenomenon of Rabi oscillations. The Rabi frequency Ω_R characterizes the strength of the coupling between the atom and the field. For a laser beam of intensity $I\left[\mathrm{W/cm^2}\right]$, the Rabi frequency is given by:

$$\Omega_R = \frac{\vec{d_{10}}\cdot\vec{\epsilon}}{\hbar}\sqrt{\frac{2I}{c\epsilon_0}}, \tag{5}$$

where d_{10} is the transition dipole moment, $\vec{\epsilon}$ is the unit vector in the direction of the electric field, and c and ϵ_0 are the speed of light and vacuum permittivity, respectively.

The probability of finding the atom in the excited state oscillates as:

$$P_1(t) = \frac{1}{2}\frac{\Omega_R^2}{\tilde{\Omega}^2}\left(1-\cos\left(\frac{\tilde{\Omega}}{t}\right)\right), \tag{6}$$

where $\tilde{\Omega} = \sqrt{\Omega_R^2+\delta^2}$ is the generalized Rabi frequency, Ω_R is the resonant Rabi frequency and δ is the detuning from resonance.

Rabi oscillations form the basis for precise state manipulation through carefully timed pulses of radiation. This can be described using the evolution of the Bloch vector in time [45, 46]:

$$\vec{v_b}(t) = \begin{pmatrix} 1 & 0 & 0 \\ 0 & \cos\theta(t) & \sin\theta(t) \\ 0 & -\sin\theta(t) & \cos\theta(t) \end{pmatrix}\cdot\vec{v_b}(0) = \Theta_{\theta(t)}\cdot\vec{v_b}(0), \tag{7}$$

where $\theta(t)$ is an integral over the Rabi frequency:

$$\theta(t) = \int_0^t \Omega_R dt'. \tag{8}$$

Two particularly important types of pulses are (Fig. 1):

π Pulse: A pulse with duration $t_\pi = \pi/\Omega_R$ (resonant case) causes a complete population inversion, transferring all atoms from $|0\rangle$ to $|1\rangle$ or vice versa. On the Bloch sphere, this corresponds to a 180° rotation around the x-axis. The effect of a π pulse on the Bloch vector can be represented by the matrix:

$$\Theta_\pi = \begin{pmatrix} 1 & 0 & 0 \\ 0 & -1 & 0 \\ 0 & 0 & -1 \end{pmatrix}. \tag{9}$$

$\pi/2$ Pulse: A pulse with duration $t_{\pi/2} = \pi/(2\Omega_R)$ creates an equal superposition of the two states. Starting from $|0\rangle$, it produces the state $\frac{1}{\sqrt{2}}(|0\rangle + |1\rangle)$. On the Bloch sphere, this corresponds to a 90° rotation around the x-axis. The effect of a $\pi/2$ pulse on the Bloch vector is given by:

$$\Theta_{\pi/2} = \begin{pmatrix} 1 & 0 & 0 \\ 0 & 0 & -1 \\ 0 & 1 & 0 \end{pmatrix}. \tag{10}$$

These pulses are fundamental building blocks in quantum control protocols, including the Ramsey interferometry sequence, which consists of two $\pi/2$ pulses separated by a free evolution period. This sequence is crucial in numerous precision measurement applications, including atomic clocks and inertial sensors. The ability to precisely control the duration, frequency, and phase of these pulses enables the intricate manipulation of quantum states, forming the basis for quantum computation and sensing protocols with atomic systems.

2.2 Two-Photon Raman Transitions

Raman transitions involve the absorption of one photon from one laser beam (pump beam) and the stimulated emission of another photon into a second laser beam (Stokes beam) to couple two atomic levels. This process is particularly useful for manipulating atomic states in quantum optics and atom interferometry experiments.

Consider a three-level atom in a laser field composed of two beams in a Λ configuration, as shown in Fig. 2. The pump beam couples levels $|1\rangle$ and $|e\rangle$, while the Stokes beam couples levels $|2\rangle$ and $|e\rangle$, resulting in a coherent coupling between $|1\rangle$ and $|2\rangle$.

To avoid resonant excitation, the detuning Δ of the Raman beams from the one-photon transition must be much larger than the linewidth Γ of $|e\rangle$. The Hamiltonian matrix for the system, in the rotating wave approximation, is given by [46]:

$$H = \frac{\hbar}{2} \begin{pmatrix} 0 & 0 & \Omega_P \\ 0 & 2\delta & \Omega_S \\ \Omega_P^* & \Omega_S^* & 2\Delta \end{pmatrix}, \tag{11}$$

where Ω_P and Ω_S are the Rabi frequencies of the pump and Stokes beams, respectively, and δ is the two-photon detuning. The Rabi frequency for transition between $|1\rangle(|2\rangle)$ and $|e\rangle$ energy levels is given

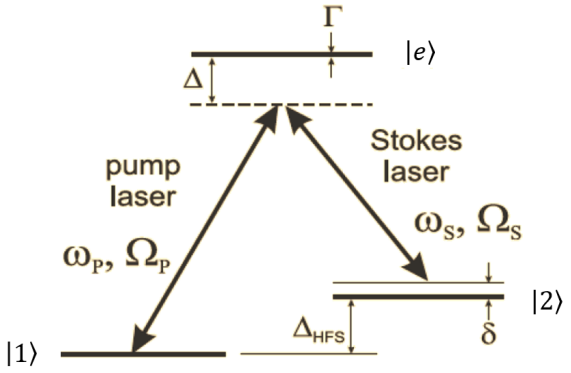

Figure 2: Raman Λ-configuration: $|1\rangle$ and $|2\rangle$ are the ground levels (separated by Δ_{HFS}) and $|e\rangle$ is the excited level, with width Γ, Δ being the detuning of the virtual level from $|e\rangle$, and δ the detuning from the two-photon resonance.

by the electric dipole interaction under the rotation wave approximation [47]:

$$\begin{aligned}\Omega_{1e} &= \frac{\langle 1|\vec{d}\cdot\vec{E}_0^-|e\rangle}{\hbar} \equiv \Omega_P \;;\; \Omega_{e1} = \frac{\langle e|\vec{d}\cdot\vec{E}_0^+|1\rangle}{\hbar} \equiv {\Omega_P}^* \\ \Omega_{2e} &= \frac{\langle 2|\vec{d}\cdot\vec{E}_0^-|e\rangle}{\hbar} \equiv \Omega_S \;;\; \Omega_{e2} = \frac{\langle e|\vec{d}\cdot\vec{E}_0^+|2\rangle}{\hbar} \equiv {\Omega_S}^*,\end{aligned} \tag{12}$$

where E_0^+ $\left(E_0^-\right)$ is the positive(negative) frequency component amplitude of the electric field and d is the dipole element. For a laser beam of intensity I [W/cm^2], the Rabi frequencies are given by:

$$\frac{|\Omega_{ie}|}{2\pi}[\mathrm{MHz}] = 70.24\left|\frac{\vec{d}_{ie}\cdot\hat{\epsilon}}{ea_0}\right|\sqrt{I}, \tag{13}$$

where $\vec{d}_{ie}$ is the dipole matrix element between states $|i\rangle$ and $|e\rangle$, $\hat{\epsilon}$ is the unit vector in the direction of the electric field, e is the elementary charge, and a_0 is the Bohr radius.

Under the condition that Δ is much larger than Ω_P and Ω_S, we can adiabatically eliminate the excited state $|e\rangle$ and reduce the system to an effective two-level system described by:

$$H_{\mathrm{eff}} = \frac{\hbar}{4\Delta}\begin{pmatrix}\Omega_P^2 & \Omega_P\Omega_S \\ \Omega_P\Omega_S & \Omega_S^2 - 4\delta\Delta\end{pmatrix}. \tag{14}$$

This effective Hamiltonian leads to Rabi oscillations between states $|1\rangle$ and $|2\rangle$ with an effective Rabi frequency:

$$\Omega_R = \frac{\Omega_P\Omega_S}{2\Delta}. \tag{15}$$

The probability of finding the atom in state $|2\rangle$, starting from state $|1\rangle$, is given by:

$$P_2(t) = 1 - P_1(t) = \left(\frac{\Omega_R}{\Omega_0}\right)^2 \sin^2\left(\frac{\Omega_0 t}{2}\right), \tag{16}$$

where the generalized Rabi frequency is given by $\Omega_0 = \sqrt{\Omega_R^2 + \delta^2}$.

2.2.1 Momentum Transfer due to Raman Transitions

The propagation direction of the two light fields, $\vec{k}_1$ and $\vec{k}_2$, and the motion of the wave packets, affect the Raman transition in three important ways:

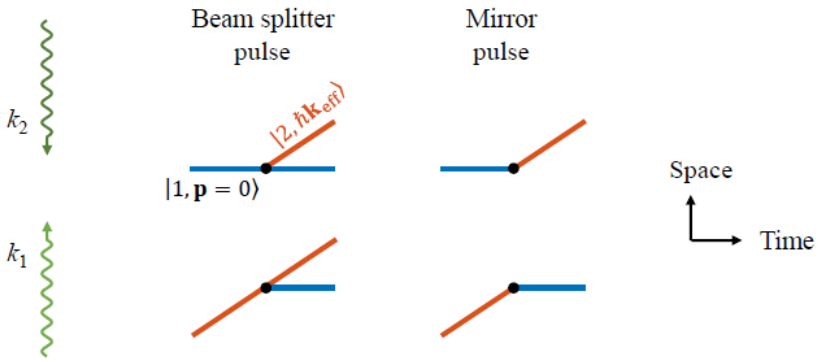

Figure 3: Counter-propagating Raman operations [48]: A space-time diagram of beam-splitting and mirror operations in the counter-propagating Raman beams configuration, for cases where the atom initially occupies $|1, \vec{p} = 0\rangle$ and $|2, \vec{p} = \hbar\vec{k}_{\text{eff}}\rangle$ in the top and bottom rows, respectively. The $|2, \vec{p} = \hbar\vec{k}_{\text{eff}}\rangle$ state is shown traveling upwards at twice the recoil velocity, $2\vec{v}_{\text{rec}} = \hbar\vec{k}_{\text{eff}}/m$.

1. The effective Rabi frequency is changed by $\Omega_R \to \Omega_R \exp\left(i\vec{k}_{\text{eff}} \cdot \vec{r}\right)$, where $\vec{k}_{\text{eff}} = \vec{k}_1 - \vec{k}_2$ and $\vec{r}$ is the position of the wave packets during the transition. Hence, the phase imprinted on the wave packets by the interaction, ϕ_Ω, picks up a factor of $\vec{k}_{\text{eff}} \cdot \vec{r}$.

2. A two-photon Doppler shift changes the two-photon detuning by $\delta \to \delta - \vec{k}_{\text{eff}} \cdot \vec{v}$, where $\vec{v}$ is the wave-packet velocity.

3. Momentum conservation during the interaction implies that the atomic states participating in the transition must have a momentum difference of $\Delta\vec{p} = \hbar\vec{k}_{\text{eff}}$.

In the counter-propagating case, which is often used in atom interferometry, $\vec{k}_{\text{eff}} \approx 2\vec{k}_1$ and the atom absorbs a photon in one direction and emits a photon in the opposite direction. In this scenario, $\Delta\vec{p}$ corresponds to twice the photon recoil velocity $\vec{v}_{\text{rec}} \simeq 2\hbar\vec{k}_1/m$, where m is the atomic mass. Hence, the states correspond to significantly different momentum states, as depicted in Fig. 3.

2.2.2 Retro-Reflection Raman Beams

Experimental convenience often involves sending both Raman beams from the same direction, while using a retro-reflecting mirror to achieve counter-propagation. When the two frequencies travel in one dimension, we label their original direction as "downward", which makes the retro-reflecting beams oriented "upward". We now have four fields at $\pm k_1$ and $\pm k_2$. Three Raman transitions are possible: the Doppler-free (simultaneously with the downward and upward pairs) and the Doppler-sensitive cases with $k_{\text{eff}} = k_1 + k_2$ or $-k_{\text{eff}} = -k_1 - k_2$.

The polarization of Raman beams determines which transition is possible, so adding polarization optics can eliminate unwanted transitions. By rotating the polarization of the beam upon retro-reflection, we can choose transitions which are either only Doppler-free or only Doppler-sensitive (Fig. 4b). Furthermore, if we use the two beams with perpendicular polarizations, we can selectively remove one with a polarizing

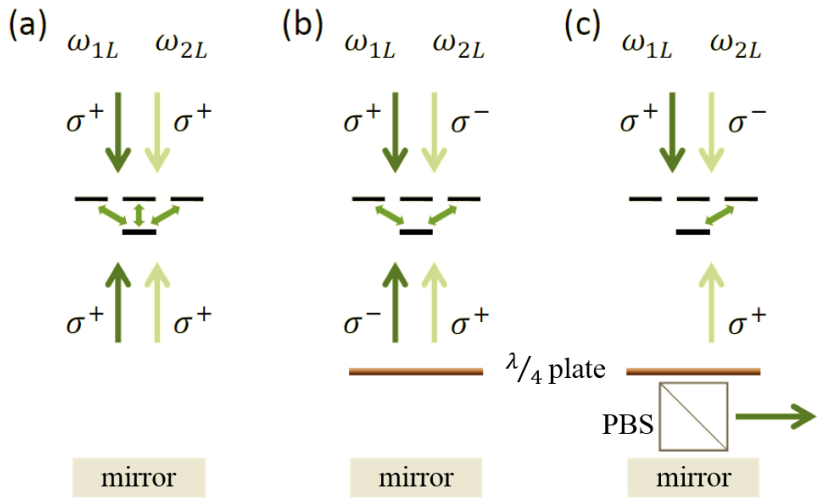

Figure 4: Raman retro-reflecting geometry [49]: A schematic representation of different realizations of Raman beam polarizations in a retro-reflecting geometry, for circular polarizations (in the lab frame). From left to right, the three optional transitions are indicated by black lines (the green two-sided arrows indicate which transition is possible): negative Doppler-sensitive, Doppler-free, and positive Doppler-sensitive. (a) All transitions are possible without polarization optics, and the beams polarizations must be identical. (b) The Doppler-free transition can be canceled by adding a $\lambda/4$ plate above the mirror, and using opposite polarizations. There will only be a Doppler-free transition if the beams are equally polarized. (c) A polarized beam splitter (PBS) is added to eliminate one retro-reflected beam. The incoming beams are oppositely polarized, so only a single Doppler-sensitive transition remains.

beam splitter (PBS) before retro-reflection (Fig. 4c).

2.2.3 Raman Transitions in Rubidium Atoms

In the context of atom interferometry with alkali atoms, Raman transitions are typically performed between the magnetically-insensitive Zeeman states ($m_F = 0$) of the two ground-state hyperfine manifolds ("clock" states), $F = 1$ and $F = 2$ in the case of ^{87}Rb, which we denote $|1\rangle$ and $|2\rangle$. Each of the two light fields Ω_1 and Ω_2 couples off-resonantly between these ground states and multiple excited state hyperfine levels, as shown in Fig. 5.

The choice of these particular "clock" states ($m_F = 0$) for Raman transitions in rubidium atoms is not arbitrary. These states are selected due to their insensitivity to first-order magnetic field fluctuations. This property is crucial in atom interferometry experiments, as it helps to minimize decoherence and systematic errors that could arise from ambient magnetic field variations. The magnetic insensitivity of these states contribute to longer coherence times and more precise measurements, which are essential for high-performance atom interferometers and atomic clocks.

In this reduced system, we adapt the effective Rabi frequency (Eq. 15) to become:

$$\tilde{\Omega}_R = \sum_i \frac{\Omega_{i,1}\Omega_{i,2}}{2(\Delta - \Delta_i)}, \tag{17}$$

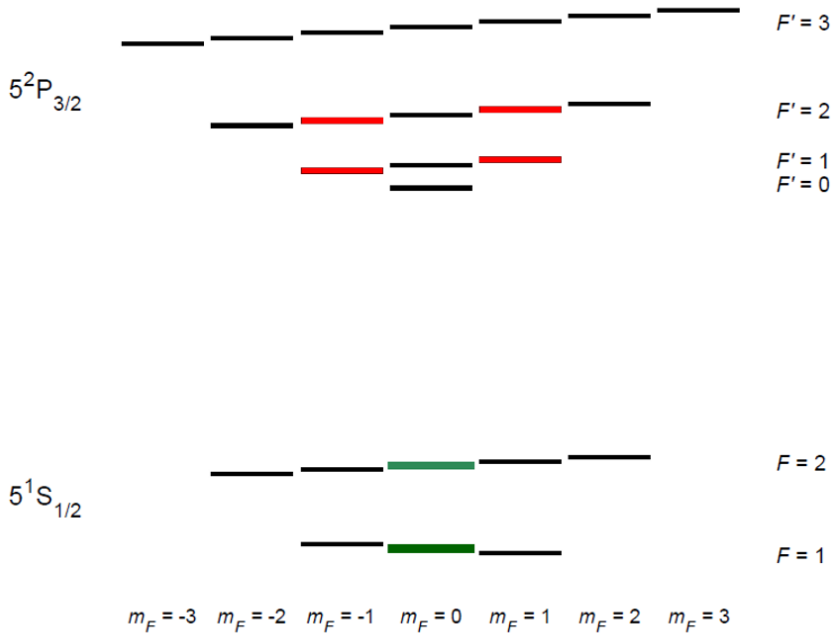

Figure 5: Raman transition in the ^{87}Rb manifold [49]: Energy level diagram of the ^{87}Rb D2 optical transition at 780nm, assuming a magnetic field is lifting the degeneracy by Zeeman shifts (not to scale). In green, the "clock" $m_F = 0$ states in the two ground-state hyperfine manifolds. In red, the excited sub-levels that can participate in the Raman transition between the clock states.

where the summation is for all the excited sub-levels that can participate in the Raman transition between the clock states.

2.3 Mach-Zehnder Atom Interferometry

The Mach-Zehnder scheme is widely used in atom interferometry, particularly for gravimetry and acceleration sensing [1]. This configuration, analogous to its optical counterpart, consists of three elements:

1. An initial $\pi/2$ beam splitter pulse, which separates the atomic wave function into its two states.
2. After a time T, a π mirror pulse, which flips the states.
3. Finally, after another time T, another $\pi/2$ pulse to mix the states and erase the which-path information.

The three-pulse Mach-Zehnder sequence is a powerful configuration for atom interferometry. It allows for high-sensitivity measurements due to the large spatial separation of the wave packets and their subsequent recombination [6]. The schematic representation of this sequence is shown in Fig. 6.

2.3.1 Interferometer Phase

The primary contribution to the Mach-Zehnder interferometer phase results from the phases imprinted on the atoms at each interaction with the Raman beams. Assuming the atom is initialized in the $|1, \vec{p} = 0\rangle$

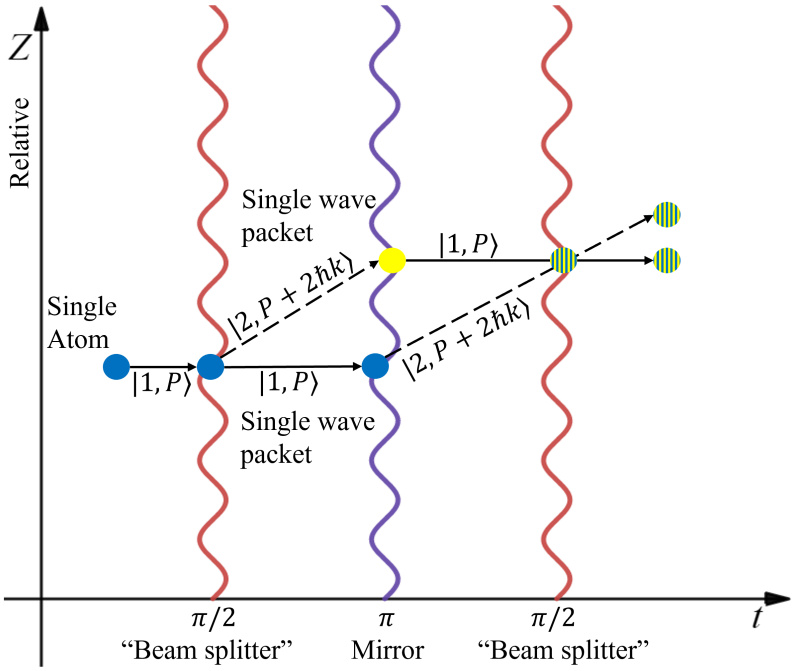

Figure 6: Mach-Zehnder atom interferometer scheme: For a two-level system, we begin at the ground state ($|1,p\rangle$), where p stands for the atom momentum. The first $\pi/2$ pulse creates an internal superposition of the $F=1$ ($|1\rangle$) and $F=2$ ($|2\rangle$) states, while adding $2\hbar k$ momentum to the upper state ($|2\rangle$). Next, we apply the π pulse, which "mirrors" the states, meaning that $|1,p\rangle \rightarrow |2,p+2\hbar k\rangle$ and $|2,p+2\hbar k\rangle \rightarrow |1,p\rangle$. When the two wave packets of each atom overlap again, we erase the 'which-path' information encoded in the momentum and spin by mixing both with a final $\pi/2$ operation. This changes each spin to two possible spin states and, likewise, each momentum to two possible momentum states. As a result, the population measured in each of the two interferometer output ports is determined by the relative phase of the two interferometer arms, allowing measurement of the relative phase.

state, following the initial $\pi/2$ pulse at $t=0$, its wave function is given by [48]:

$$\Psi(0) = \frac{1}{\sqrt{2}}\left(|1,\vec{p}=0\rangle + ie^{-i\vec{k}_{\text{eff}}\cdot\vec{r}_1}|2,\vec{p}=\hbar\vec{k}_{\text{eff}}\rangle\right), \tag{18}$$

where $\vec{r}_1$ denotes the classical position of the atoms at $t=0$. After the π pulse at $t=T$ the wave function becomes:

$$\Psi(T) = \frac{1}{\sqrt{2}}\left(ie^{-i\vec{k}_{\text{eff}}\cdot\vec{r}_2}|2,\vec{p}=\hbar\vec{k}_{\text{eff}}\rangle - e^{-i\vec{k}_{\text{eff}}\cdot(\vec{r}_3-\vec{r}_1)}|1,\vec{p}=0\rangle\right), \tag{19}$$

where $\vec{r}_2$ and $\vec{r}_3$ are, respectively, the positions of the atom in the lower and upper interferometer paths at $t=T$. Finally, following the second $\pi/2$ pulse at $t=2T$, the wave functions are mixed to produce:

$$\begin{aligned}\Psi(2T) = -\frac{1}{2}\Big[&\left(e^{-i\vec{k}_{\text{eff}}\cdot(\vec{r}_1-\vec{r}_3)} + e^{-i\vec{k}_{\text{eff}}\cdot(\vec{r}_2-\vec{r}_4)}\right)|1,\vec{p}=0\rangle \\ &+ie^{-i\vec{k}_{\text{eff}}\cdot\vec{r}_4}\left(e^{-i\vec{k}_{\text{eff}}\cdot(\vec{r}_1-\vec{r}_3)} - e^{-i\vec{k}_{\text{eff}}\cdot(\vec{r}_2-\vec{r}_4)}\right)|2,\vec{p}=\hbar\vec{k}_{\text{eff}}\rangle\Big],\end{aligned} \tag{20}$$

where $\vec{r}_4$ is the common position of the atom at $t = 2T$. At the end of the interferometer sequence, we thus have the probabilities to find the atom in each of its internal states:

$$\begin{aligned} P_1 &= \left| \frac{1}{2} \left(e^{-i\vec{k}_{\text{eff}} \cdot (\vec{r}_1 - \vec{r}_3)} + e^{-i\vec{k}_{\text{eff}} \cdot (\vec{r}_2 - \vec{r}_4)} \right) \right|^2 = \frac{1}{2}(1 + \cos\phi) \\ P_2 &= \left| \frac{1}{2} \left(e^{-i\vec{k}_{\text{eff}} \cdot (\vec{r}_1 - \vec{r}_3)} - e^{-i\vec{k}_{\text{eff}} \cdot (\vec{r}_2 - \vec{r}_4)} \right) \right|^2 = \frac{1}{2}(1 - \cos\phi), \end{aligned} \tag{21}$$

with the interferometer phase:

$$\phi = \vec{k}_{\text{eff}} \cdot (-\vec{r}_1 + \vec{r}_2 + \vec{r}_3 - \vec{r}_4). \tag{22}$$

We notice that the expression for ϕ (Eq. 22) resembles a discrete second-order derivative of the atom position through the interferometer time. By assuming that the atom experiences a constant acceleration $\vec{a}$, we get:

$$\phi = -\vec{k}_{\text{eff}} \cdot \vec{a} T^2. \tag{23}$$

For the specific case of pure free fall and Raman beams which are aligned vertically, we get $\phi = k_{\text{eff}} g T^2$, which indicates that such an interferometer scheme can determine g with high resolution.

The interrogation time T plays a crucial role in determining the sensitivity of the interferometer. As seen in Eq. 23, the phase shift scales quadratically with T. This implies that longer interrogation times lead to larger phase shifts and, consequently, higher sensitivity to accelerations and rotations (Sec. 2.3.2). However, increasing T also presents practical challenges. The atomic cloud expands during the interrogation time, potentially leading to a reduced signal-to-noise ratio due to decreased atomic density. Additionally, longer interrogation times make the interferometer more susceptible to environmental perturbations and decoherence effects. Therefore, the choice of T requires a careful balance between sensitivity and experimental constraints.

A more general approach to determine the interferometer phase is by considering the space-time area $\vec{A}$ enclosed by the interfering arms:

$$\vec{A} = \int \Delta\vec{r}(t) dt, \tag{24}$$

where $\Delta\vec{r}$ is the spatial separation between the arms. For a constant acceleration $\vec{a}$, the phase shift is given by [48]:

$$\phi_{\vec{a}} = -\frac{m}{\hbar} \vec{a} \cdot \vec{A}. \tag{25}$$

Similarly, the spatial, or vector, area enclosed by the interferometer arms is given by:

$$\vec{\mathcal{A}} = \frac{1}{2} \oint \vec{r} \times d\vec{r}, \tag{26}$$

which gives rise to an interferometer phase related to a rotating motion of the atoms:

$$\phi_{\vec{\Omega}} = \frac{2m}{\hbar} \vec{\Omega} \cdot \vec{\mathcal{A}}, \tag{27}$$

where $\vec{\Omega}$ is the rotation velocity. This phase is equivalent to the Sagnac phase shift [50]:

$$\phi_{\text{Sagnac}} = \frac{2E}{\hbar c^2} \vec{\Omega} \cdot \vec{\mathcal{A}}, \tag{28}$$

where E is the energy of the interfering particles. For atoms, we can use $E = mc^2$, which makes Eq. 27 and Eq. 28 equivalent. The Sagnac effect, originally discovered for light interferometers, manifests in atom interferometers due to the wave nature of matter. The key difference is that the phase shift for atoms is proportional to their mass, potentially leading to much higher sensitivities compared to optical interferometers.

This space-time area approach provides a powerful framework for understanding and calculating the phase shifts in various atom interferometer configurations, connecting the classical Sagnac effect to quantum matter-wave interferometry. In the following section, we will explore how this framework applies specifically to rotation sensing in Mach-Zehnder atom interferometers.

2.3.2 Rotation Sensing

The Mach-Zehnder atom interferometer becomes sensitive to rotations when the two interfering paths enclose a spatial area. This occurs when the atoms have a velocity component perpendicular to $\vec{k}_{\text{eff}}$. In this case, the rotation phase can be expressed as:

$$\phi_{\vec{\Omega}} = 2\vec{\Omega} \cdot (\vec{v} \times \vec{k}_{\text{eff}})T^2, \tag{29}$$

where $\vec{v}$ is the average velocity of the atoms during the interferometer sequence. This equation is equivalent to the Sagnac phase shift derived in the previous section (Eqs. 27-28), with the enclosed area $\vec{\mathcal{A}}$ now explicitly given by $(\vec{v} \times \vec{k}_{\text{eff}})T^2$. A unique feature of rotation sensing in atom interferometry is the explicit dependence on the velocity of the atoms. This factor introduces both challenges and opportunities:

1. Velocity-dependent phase: The rotation phase varies with the atomic velocity, requiring careful consideration of the velocity distribution in the atomic ensemble.

2. Velocity selection: The velocity dependence allows for selective probing of specific velocity classes within the atomic ensemble, potentially enhancing the signal-to-noise ratio.

3. Multi-axis sensing: By manipulating the direction of $\vec{k}_{\text{eff}}$ and the atomic velocity distribution, it is possible to create interferometers sensitive to rotations around different axes.

In practical implementations, the output signal of the interferometer must be averaged over the velocity distribution of the atomic ensemble. This averaging process can impact the overall sensitivity and dynamic range of the rotation sensor.

The ability to measure rotations using atom interferometry lays the foundation for a wide range of applications, from inertial navigation systems to tests of fundamental physics. In the following sections, we will explore specific implementations and techniques that leverage high-level rotation sensitivity, including the point source interferometry method that forms the focus of our research.

While the Mach-Zehnder configuration provides a powerful tool for rotation sensing, its sensitivity to initial atomic velocities limits its practical applications. In the next section, we will explore an alternative approach, the Point Source Interferometry (PSI) method [43, 51, 52], which addresses some of these challenges and forms the core of our research.

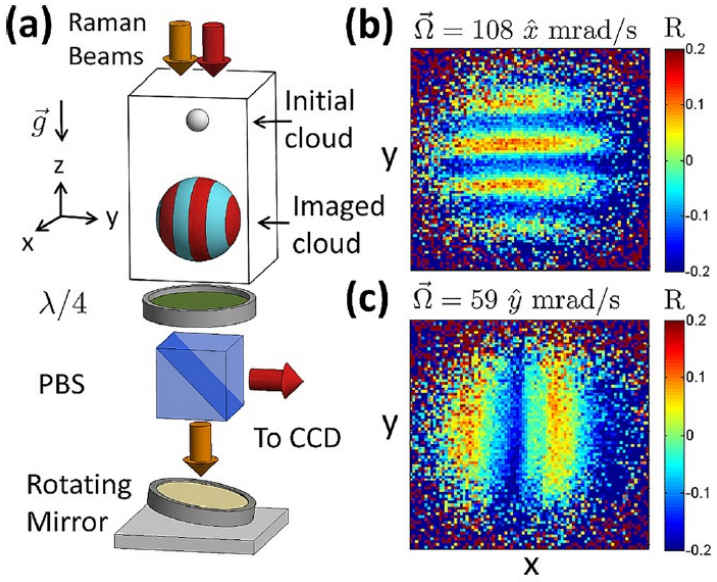

Figure 7: The PSI experiment [53]: (a) The initial atom cloud is prepared and then released into free fall while interacting with Raman beams to undergo an interferometer sequence made of $\pi/2 - \pi - \pi/2$ pulses. One of the beams is reflected from the rotating mirror, which simulates a rotation in the frame of the atom. After the atom falls for some time, and the cloud has expanded, it is imaged (the image beam is deflected to the CCD camera by the polarized beam-splitter, PBS, after passing through a quarter-wave plate, $\lambda/4$) and the fringe pattern is captured. (b) and (c) are examples of fringe patterns for different rotations of the mirror.

2.4 Point Source Interferometer

The Point Source Interferometer (PSI) is a specific implementation of light-pulse atom interferometry that offers unique advantages for rotation sensing. First introduced by Dickerson et al. [43], PSI utilizes a single expanding cloud of cold atoms to measure rotations by probing the spatial frequency of the atomic density in a given output internal atomic state.

2.4.1 Principle of Operation

The PSI method (Fig. 7) exploits the correlation between position and velocity generated by the expansion of an initially compact atomic cloud throughout the interferometer sequence. When the final cloud size significantly exceeds its initial size, each atom's final position, $\vec{x}$, is essentially dictated by its initial thermal velocity, $\vec{v}$. This allows for the approximation $\vec{x} \approx \vec{v}T_{\text{ex}}$, where T_{ex} represents the total expansion time.

In the ideal case of a perfect point source, where all atoms originate from the same point in space, the Sagnac phase becomes [51]:

$$\Delta\Phi_{\Omega,\text{PS}} = \frac{2T_R^2}{T_{\text{ex}}}(\vec{k}_{\text{eff}} \times \vec{\Omega}) \cdot \vec{x} \equiv \vec{k}_x \cdot \vec{x}, \tag{30}$$

where T_R is the Ramsey time between interferometer pulses, $\vec{k}_{\text{eff}}$ is the effective wave vector of the Raman beams, and $\vec{\Omega}$ is the rotation rate.

However, in real experiments, the atomic cloud has a finite initial size and can be approximated by a Gaussian spacial distribution. For a cloud with an initial Gaussian spatial distribution of width σ_{x0} and a Gaussian velocity distribution of width σ_{v0}, the phase-space density at time t is given by:

$$\rho(x, v, t) \propto \exp\left(-\frac{1}{2}\left[\frac{(x - vt)^2}{\sigma_{x0}^2} + \frac{v^2}{\sigma_{v0}^2}\right]\right). \tag{31}$$

This finite initial size affects both the fringe pattern and the contrast of the interferometer. The probability of finding an atom in a particular internal state $|s\rangle$ at position $\vec{x}$ becomes [54]:

$$P_s(\vec{x}) = \frac{1}{2}[1 + C\cos\Big(\alpha\vec{k}_x \cdot \vec{x} + \phi_s\Big)], \tag{32}$$

where C is the fringe contrast, $\alpha = 1 - \sigma_{x0}^2/\sigma_f^2$ accounts for the finite initial size of the cloud, $\sigma_f = \sqrt{\sigma_{x0}^2 + T_{\text{ex}}^2\sigma_{v0}^2}$ is the final cloud size, and ϕ_s is a phase offset determined by gravity and platform acceleration. The contrast C is given by:

$$C = C_0 \cdot \exp\left[-\frac{1}{2}k_x^2\sigma_{x0}^2\left(1 - \frac{\sigma_{x0}^2}{\sigma_f^2}\right)\right], \tag{33}$$

where C_0 is the base contrast of the interferometer.

These equations highlight several key differences between the ideal point-source case and the realistic Gaussian cloud:

1. Fringe periodicity: In the Gaussian case, the fringe periodicity is modified by the factor α, which approaches 1 as the cloud expands ($\sigma_f \gg \sigma_{x0}$).

2. Contrast: The contrast decreases with increasing k_x and σ_{x0}, limiting the maximum detectable rotation rate.

3. Position-velocity correlation: The finite initial size introduces imperfections in the position-velocity correlation, affecting the overall sensitivity of the interferometer.

Understanding these differences is crucial for optimizing PSI performance and accurately interpreting experimental results. The interplay between initial cloud size, expansion time, and fringe periodicity determines the sensitivity and dynamic range of the PSI, which we will discuss in more detail in subsequent sections.

2.4.2 Advantages and Limitations

The PSI method offers several advantages over traditional Mach-Zehnder atom interferometers:

1. Single-source operation: PSI requires only one atomic cloud, simplifying the experimental setup compared to dual-cloud interferometers [55–58].

2. Multi-axis sensing: By analyzing the fringe pattern in different directions, PSI can simultaneously measure rotations around multiple axes [43].

3. Compact design: The expanding cloud geometry allows for the use of a more compact device, as opposed to large-area atom interferometers [51].

However, PSI also faces some limitations:

1. Finite dynamic range: The measurable rotation rates are bounded by the condition that the fringe spacing must be larger than the initial cloud size and smaller than the final cloud size.

2. Velocity-dependent sensitivity: The sensitivity varies across the atomic cloud due to the position-velocity correlation.

2.4.3 Sensitivity and Dynamic Range

The sensitivity of a PSI to rotations, limited by projection noise, is given by [59]:

$$\delta\Omega = \frac{T_{\mathrm{ex}}/T_R^2}{2C\sqrt{N\nu/2}k_{\mathrm{eff}}\sigma_f}, \tag{34}$$

where N is the number of atoms per operation and ν is the frequency of operations.

While sensitivity is crucial for precise measurements, the range of rotations that can be detected is equally important for practical applications. This range, known as the dynamic range, is determined by the minimum and maximum detectable rotation rates.

The PSI method differs from traditional interferometric rotation sensors in several key aspects:

1. Measurement quantity: In traditional sensors, the Sagnac phase is directly measured and typically shows a linear correlation with rotation. In PSI, the spatial frequency of interference fringes is measured.

2. Smallest detectable rotation: For traditional sensors, this is determined by the smallest measurable phase difference. In PSI, it is set by the condition $k_x\sigma_f \gtrsim 1$, ensuring that the cloud size exceeds the period of spatial oscillation.

3. Maximum detectable rotation: In PSI, this is limited by the condition $k_x\sigma_{x0} \gtrsim 1$, where the fringe period becomes larger than the initial cloud size, causing diminishing contrast.

4. Dynamic range: For PSI, this is constrained to $1/\sigma_f \lesssim k_x \lesssim 1/\sigma_{x0}$, leading to the following limits:

$$\Omega_{\mathrm{min}} \sim \frac{T_{\mathrm{ex}}/T_R^2}{2k_{\mathrm{eff}}\sigma_f} \quad ; \quad \Omega_{\mathrm{max}} \sim \frac{T_{\mathrm{ex}}/T_R^2}{2k_{\mathrm{eff}}\sigma_{x0}}, \tag{35}$$

   resulting in a dynamic range ratio of $\Omega_{\mathrm{max}}/\Omega_{\mathrm{min}} \sim \sigma_f/\sigma_{x0}$.

5. Relationship between sensitivity and minimum detectable rate: In PSI, $\delta\Omega/\Omega_{\mathrm{min}} \approx 1/\sqrt{N/2}$, suggesting that the sensitivity (uncertainty) can be much smaller than the minimum detectable rate.

It should be noted that these limits and relationships are approximations and can vary, depending on the specific image analysis method used, such as ellipse fitting [60], phase shear [61], or phase map [62] techniques.

2.4.4 Quantum Derivation of PSI

To gain a deeper understanding of the PSI, we can derive its behavior from a quantum mechanical perspective. Consider an initial wave function $\psi(\vec{r})$ subject to a sequence of splitting and recombining pulses $\pi/2 - \pi - \pi/2$ with an initial state $|0\rangle$ and another state $|1\rangle$. In the inertial frame, the initial pulse applies a momentum transfer k_{eff} in the $\hat{z}$ direction to the state $|1\rangle$. The subsequent pulses apply momentum kicks in directions that evolve due to rotation. For small rotation rates ($\Omega T_R \ll 1$), we can approximate the dynamics along the $\hat{x}$ direction. The two paths end up with the same velocity but at different positions:

$$x_{|1\rangle-|0\rangle} = x_0 + 2v_0T_R - v_R\Omega T_R^2, \quad x_{|0\rangle-|1\rangle} = x_0 + 2v_0T_R + v_R\Omega T_R^2, \tag{36}$$

where $v_R = \hbar k_{\text{eff}}/m$ is the recoil velocity. The phase difference between the two paths due to the velocity difference in the x-direction is:

$$\delta\phi_{\text{rot}} = \frac{m}{2\hbar}[(v_0 - v_R\Omega T_R)^2 - (v_0 + v_R\Omega T_R)^2]T_R = -2k_{\text{eff}}v_0\Omega T_R^2, \tag{37}$$

which is consistent with our earlier derivation of the rotation phase (Eq. 30).

The final wave function in the state $|0\rangle$ after the sequence is:

$$\psi_f(x) = \frac{1}{\sqrt{2}}[\psi_\sigma(x - x_a) + \psi_\sigma(x - x_b)e^{-i\delta\phi_{\text{rot}}}], \tag{38}$$

where x_a and x_b are the final positions of the two paths, and ψ_σ is the wave function after expansion from an initial width σ_0 to a final width σ after time $t = 2T_R$. It follows that the final wave function is similar to the result of an expansion starting with two Gaussian wave packets centered at a relative distance $d = |x_a - x_b| = 2v_R\Omega T_R^2$, leading to the emergence of a fringe pattern in a manner equivalent to the double-slit experiment. Here, the distance d is proportional to the square of the interferometer time. Still, the fringe periodicity depends on the total expansion time since the wave packet was of minimal size.

The evolution of a Gaussian wave-packet in free space, or a quadratic potential, can be expressed in terms of the evolution of the width σ. The simplified expression for one dimension in the frame moving with the center of the wave-packet is given by [63, 64]:

$$\psi_\sigma(x,t) = \frac{\psi_0[x/\lambda(t)]}{\sqrt{\lambda(t)}} \exp\left(\frac{im}{2\hbar}\frac{\dot{\sigma}}{\sigma}x^2\right), \tag{39}$$

where $\psi_0(x)$ is the initial wave-packet wave function and $\lambda(t) = \sigma(t)/\sigma(0)$. The evolution of the width of a Gaussian wave-packet in free space is given by:

$$\sigma(t) = \sqrt{\sigma(0)^2 + \hbar^2t^2/4m^2\sigma(0)^2} = \sqrt{\sigma_{x0}^2 + \sigma_{v0}^2t^2}\,, \tag{40}$$

with $\sigma_{v0} = \hbar/2m\sigma_{x0}$ for a coherent Gaussian wave-packet.

The phase difference between the two wave functions at a given point x follows from the quadratic phases of the expanding Gaussians of the form of Eq. 39 and is given by:

$$\delta\phi(x) = \frac{m\dot{\sigma}}{2\hbar\sigma}[(x - v_R\Omega T_R^2)^2 - (x + v_R\Omega T_R^2)^2] = -k_\Omega x, \tag{41}$$

where $k_\Omega = 2(\dot{\sigma}/\sigma)k_{\text{eff}}\Omega T_R^2$.

For a Gaussian wave-packet with an initial width σ_0, we obtain:

$$k_\Omega = 2k_{\text{eff}}\Omega\frac{T_R^2}{T_{\text{ex}}}\left(1-\frac{\sigma_0^2}{\sigma_f^2}\right), \tag{42}$$

which is equivalent to the semi-classical result of Eq. 30 in the limit of long expansion times ($\sigma_f \gg \sigma_0$), as well as the well-known double-slit interference wave vector $k_\Omega = md/\hbar T_{ex}$.

The contrast is obtained by observing the amplitude of the interference term from Eqs. 38-39:

$$\exp\left[-\frac{(x-d/2)^2}{4\sigma_f^2}-\frac{(x+d/2)^2}{4\sigma_f^2}\right] = e^{-x^2/2\sigma_f^2}e^{-d^2/8\sigma_f^2}, \tag{43}$$

from which it follows that the contrast is:

$$C = \exp\left(-\frac{1}{2}k_\Omega^2\frac{\sigma_0^2}{1-\sigma_0^2/\sigma_f^2}\right), \tag{44}$$

which is consistent with our earlier derivation (Eq. 33).

While the above derivation assumes a pure Gaussian state, in real experiments we often deal with thermal clouds. A thermal cloud could be modelled as a mixture of states. For example, a thermal cloud in an initial harmonic trap is a mixture of Hermite-Gaussian states:

$$\rho(x,x') = \sum_n w_n\Phi_n(x)\Phi_n^*(x'), \tag{45}$$

where n is the number of nodes in the function and runs from 0 to ∞ and $w_n \propto \exp(-n\hbar\omega/k_BT)$ are the weights (probabilities) of the states $|n\rangle$. It is clear that a thermal Boltzmann distribution yields a Gaussian spatial distribution $\sum_n w_n|\Phi_n(x)|^2 \propto \exp\left(-x^2/2\sigma_T^2\right)$ with $\sigma_T = \sqrt{k_BT/m\omega^2}$ in a harmonic trap. It follows that for a thermal distribution σ_0 in Eq. 44 can be replaced by the width of the thermal distribution to obtain the right expression for the contrast of an interferometer with a thermal cloud. This expression for the contrast is identical to the expression appearing in [65].

This quantum mechanical derivation provides a more fundamental understanding of the PSI, confirming and extending the semi-classical results presented earlier. It offers insights into the origin of the fringe pattern, the impact of wave packet evolution on the interferometer's performance, and the effects of finite temperature on the contrast. The consistency between this quantum approach and the semi-classical treatment underscores the robustness of the PSI method. Moreover, this derivation lays the groundwork for further refinements and optimizations of PSI-based rotation sensors, particularly in scenarios where quantum effects become significant. As we move towards more precise and compact atom interferometers, such quantum mechanical considerations will play an increasingly crucial role in pushing the boundaries of rotation sensing capabilities.

3 Noise Mitigation

In atom interferometers based on Raman transitions (Sec. 2.2), such as the point source interferometry (PSI, Sec. 2.4), the phase difference between the two Raman lasers is imprinted on the phase of the atomic wave function at each pulse. As this phase difference depends on the position of the atoms, the interferometer is sensitive to inertial forces and can thus measure rotation rates and accelerations (Sec. 2.3). However, a drawback of this technique is that the measurement of the interferometric phase is affected by the phase noise of the Raman lasers as well as parasitic vibrations. This section analyzes the primary noise sources affecting our PSI system and presents methods and considerations for mitigating their effects.

3.1 Theory of Noise Sources

The phase sensitivity of an atom interferometer, defined as the uncertainty σ_ϕ of the phase measurement per shot, is affected by both the phase noise of the Raman lasers and seismic effects. In this section, we provide an analytical analysis of these sources, which directly influence the phase noise in measurements. These types of noise simply add to the measured phase, making it straightforward to calculate their effect on the interferometer sensitivity.

3.1.1 Laser Phase Noise

Laser phase noise is a critical factor limiting the sensitivity of atomic interferometers. It arises from instabilities in the relative phase of the Raman beams, which are imprinted on the atoms during each interferometer pulse. To quantify the effect of laser phase noise, we employ the formalism of the sensitivity function introduced by Cheinet et al. [66].

The sensitivity function $g(t)$ characterizes how the interferometer phase Φ responds to fluctuations in the Raman laser phase ϕ at time t during the interferometer sequence. It is defined as:

$$g(t) = 2 \lim_{\delta\phi \to 0} \frac{\delta P(\delta\phi, t)}{\delta\phi}, \tag{46}$$

where $\delta P(\delta\phi, t)$ is the change in transition probability due to a small phase step $\delta\phi$ applied at time t. For a Mach-Zehnder $\pi/2 - \pi - \pi/2$ pulse sequence (Sec. 2.3) with total interrogation time $2T$, we choose the time origin at the middle of the π pulse. Thus, we have $t_i = -(T + 2\tau_R)$ and $t_f = (T + 2\tau_R)$, where τ_R is the duration of a $\pi/2$ pulse (Sec. 2.1.2). For this case, we find that the sensitivity function of Eq. 46 is an odd function, with its expression for $t > 0$ given by:

$$g(t) = \begin{cases} \sin(\Omega_R t) & 0 < t < \tau_R \\ 1 & \tau_R < t < T + \tau_R \\ -\sin(\Omega_R (T - t)) & T + \tau_R < t < T + 2\tau_R \end{cases}, \tag{47}$$

where Ω_R is the Rabi frequency. The interferometer phase fluctuations due to laser phase noise can then be calculated as:

$$\delta\Phi = \int_{-\infty}^{\infty} g(t) \frac{d\phi(t)}{dt} dt. \tag{48}$$

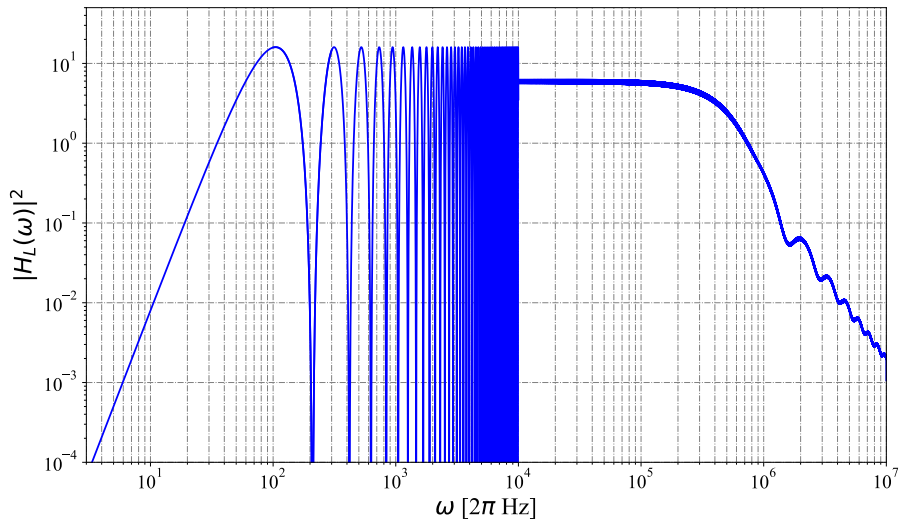

Figure 8: Laser-phase transfer function: Plot of the laser-phase transfer function $|H_L(\omega)|^2$ (see Eq. 50 and $H(\omega) = \omega G(\omega)$) calculated for Ramsey time of $T = 30\,\text{ms}$ and Rabi frequency of $\Omega_R = 2\pi \cdot 50\,\text{kHz}$. For angular frequencies above $2\pi \cdot 7\,\text{kHz}$ a moving average was used.

To analyze the frequency-dependent response of the interferometer to phase noise, we consider a sinusoidal phase modulation $\phi(t) = A_0 \cos(\omega_0 t + \varphi)$. The resulting phase shift is:

$$\delta\Phi = -A_0\omega_0 \text{Im}[G(\omega_0)] \cos(\varphi), \tag{49}$$

where $G(\omega)$ is the Fourier transform of $g(t)$:

$$G(\omega) = \frac{4i\Omega_R}{\omega^2 - \Omega_R^2} \sin\left(\frac{\omega(T+2\tau_R)}{2}\right)\left(\cos\left(\frac{\omega(T+2\tau_R)}{2}\right) + \frac{\Omega_R}{\omega}\sin\left(\frac{\omega T}{2}\right)\right). \tag{50}$$

The transfer function $H(\omega) = \omega G(\omega)$ characterizes how phase noise at different frequencies affects the interferometer, as shown in Fig. 8. Key features of this function include:

- Zeros at frequencies $f_k = k/(T + 2\tau_R)$, where k is an integer.
- Low-pass behavior with an effective cut-off frequency $f_0 = (\sqrt{3}/3)(\Omega_R/2\pi)$.
- ω^{-1} dependence for $\omega \ll \Omega_R$ and ω^{-2} for $\omega \gg \Omega_R$

The sensitivity of the interferometer is characterized by the Allan variance of the phase fluctuations:

$$\sigma_\Phi^2(\tau) = \frac{1}{\tau}\sum_{n=1}^{\infty} |H(2\pi n f_c)|^2 S_\phi(2\pi n f_c), \tag{51}$$

where $f_c = 1/T_c$ is the cycle frequency of the interferometer and $S_\phi(\omega)$ is the power spectral density of the laser phase noise. This equation shows that the sensitivity is limited by an aliasing phenomenon similar to the Dick effect in atomic clocks [67], where only the phase noise at multiples of the cycling frequency contributes to the Allan variance.

For the simple case of white Raman phase noise, where $S_\phi(\omega) = S_\phi^0$, Eq. 51 simplifies to:

$$\sigma_{\Phi,0}^2(\tau) = \left(\frac{\pi}{2}\right)^2 \frac{S_\phi^0}{\tau}\frac{T_c}{\tau_R}. \tag{52}$$

In this scenario, the sensitivity of the interferometer depends not only on the Raman phase noise spectral density but also on the pulse duration τ_R. Intuitively, one might think that using the largest possible pulse duration would yield better sensitivity. However, in the counter-propagating configuration of Raman transitions (Sec. 2.2), longer pulses increase velocity selectivity, potentially reducing the number of atoms contributing to the signal. This reduction can increase the detection noise contribution, creating a trade-off. Consequently, there exists an optimum value of τ_R that depends on the specific experimental parameters. For our PSI system, we found this optimum to be approximately $\tau_R \simeq 5\mu$s."

Minimizing laser phase noise is crucial for achieving high sensitivities. This typically involves phase locking the Raman lasers to a low-noise microwave reference. The overall laser phase noise is influenced by several factors, including:

- Reference oscillator noise.
- Noise from the microwave frequency synthesis chain.
- Residual noise from the laser phase-lock loop.
- Noise from optical fibers and other optical elements.

Each noise source must be carefully characterized and minimized to optimize the interferometer's performance. Techniques such as using ultra-low noise quartz oscillators, optimized phase-lock loop designs, and vibration isolation of critical optical components, are employed to reduce the overall laser phase noise [68, 69].

In conclusion, a thorough understanding of laser phase noise and its impact on atom interferometers is essential for pushing the boundaries of measurement sensitivity. By carefully analyzing the transfer function and minimizing various noise sources, we can design and implement more precise and accurate atomic sensors for a wide range of applications. In the next section, we will make a thorough analysis of the effect of seismic noise of the optical elements on the interferometer phase.

3.1.2 Seismic Noise

Mechanical vibrations of optical elements, particularly the retro-reflecting mirror (Sec. 2.2.2), introduce phase noise between the Raman beams. This noise directly impacts the interferometer phase. If separate optical elements are used to guide the Raman beams into the physics chamber, the whole apparatus needs to be isolated from vibrations, as illustrated in Fig. 9a. When the same optical elements are used for both Raman beams and a retro-reflecting mirror, vibrations from most optical elements are common-mode and cancel out. As shown in Fig. 10, phase noise is only induced by vibrations of the retro-reflecting mirror, and therefore, only this mirror has to be isolated against vibrations from the floor (Fig. 9b).

The same formalism used for the laser phase noise (Sec. 3.1.1) can be used to evaluate the interferometer phase noise due to parasitic vibrations caused by the movement of the retro-reflecting mirror. Here, we decided to show another approach by analyzing the Mach-Zehnder interferometer phase of Eq. 22. We

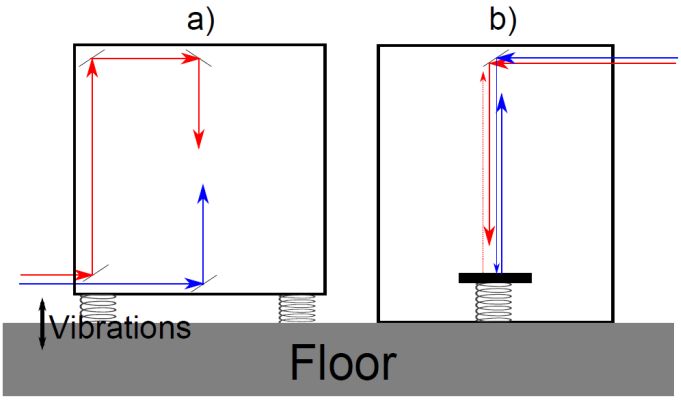

Figure 9: Schemes for suppressing vibration induced Raman phase noise [70]: Illustrated here are two different frequency components (blue, red) to drive Doppler-sensitive Raman transitions depending on their propagation direction. (a) A system where the beams are guided separately. (b) A system utilizing a retro-reflecting mirror, as described in Sec. 2.2.2.

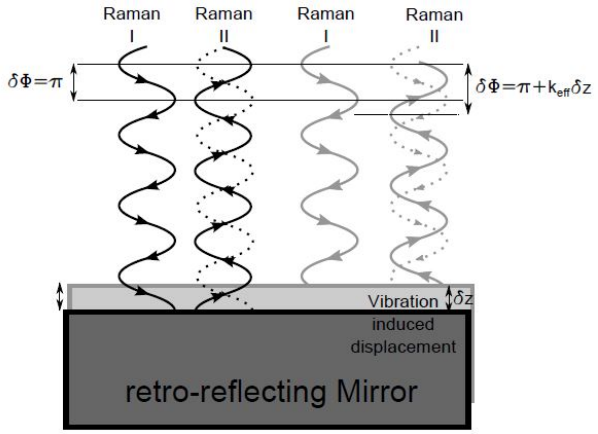

Figure 10: Vibration-induced Raman phase noise from retro-reflecting mirror [70]: The black and gray lines illustrate the propagation of the two Raman beams. Vibrations induce a displacement of δz, which leads to a phase difference of $k_{\text{eff}}\delta z$ in the gray lines, relative to the black lines, which is the no-vibration case.

can express the phase including the effect of mirror vibrations as:

$$\begin{aligned}\phi &= \vec{k}_{\text{eff}} \cdot (-[\vec{r}_1 - \vec{r}_m(0)] + [\vec{r}_2 - \vec{r}_m(T)] + [\vec{r}_3 - \vec{r}_m(T)] - [\vec{r}_4 - \vec{r}_m(2T)]) \\ &= \vec{k}_{\text{eff}} \cdot [-\vec{r}_1 + \vec{r}_2 + \vec{r}_3 - \vec{r}_4] - \vec{k}_{\text{eff}} \cdot [-\vec{r}_m(0) + 2\vec{r}_m(T) - \vec{r}_m(2T)]\,, \end{aligned} \tag{53}$$

where $\vec{r}_m(t)$ is the position of the mirror at time t. The first term in brackets represents the ideal interferometer phase ϕ_a as in Eq. 23, while the second term represents the vibration-induced phase ϕ_{vib}.

The contribution of vibration phase noise $\sigma_{\phi,vib}$ can be quantified as

$$\sigma^2_{\phi,\text{vib}} = \int_0^\infty |H_{\text{vib}}(\omega)|^2 S_{\text{vib}}(\omega) d\omega, \tag{54}$$

where $S_{\text{vib}}(\omega)$ is the power spectral density (PSD) of vibrations and $H_{\text{vib}}(\omega)$ is the vibration transfer function of the interferometer. To derive $H_{\text{vib}}(\omega)$, we assume a vertical oscillatory perturbation to the

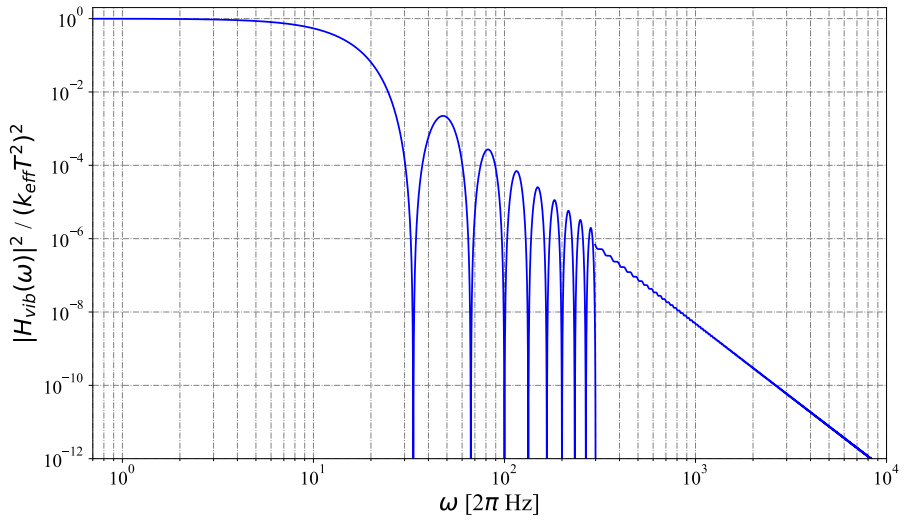

Figure 11: Vibration transfer function: Plot of the vibration transfer function $|H_{\mathrm{vib}}(\omega)|^2$ (Eq. 58) scaled by $\left(k_{\mathrm{eff}}T^2\right)^2$ calculated for Ramsey time of $T = 30\,\mathrm{ms}$. For angular frequencies above $2\pi \cdot 300\,\mathrm{Hz}$ a moving average was used.

mirror with frequency ω:

$$a_{m,\omega}(t) = a_{\omega,c}\cos[\omega(t-T)] + a_{\omega,s}\sin[\omega(t-T)]. \tag{55}$$

Integrating twice to find the vertical position of the mirror $z_{m,\omega}(t)$, we get:

$$z_{m,\omega}(t) = z_0 + v_0 t - \frac{1}{\omega^2}a_{m,\omega}(t), \tag{56}$$

and substituting into the expression for ϕ_{vib} from Eq. 53, we obtain that the contributions of z_0 and v_0, as well as the sine component ($a_{\omega,s}$), vanish, such that:

$$\phi_{\mathrm{vib},\omega} = \frac{4k_{\mathrm{eff}}a_{\omega,c}}{\omega^2}\sin^2\left(\frac{\omega T}{2}\right). \tag{57}$$

From this, we can derive the transfer function:

$$|H_{\mathrm{vib}}(\omega)| = \frac{4k_{\mathrm{eff}}}{\omega^2}\sin^2\left(\frac{\omega T}{2}\right). \tag{58}$$

This transfer function, illustrated in Fig. 11, exhibits several key features:

- Constant sensitivity for low frequencies ($\omega \lesssim 2/T$).
- $1/\omega^2$ decrease at higher frequencies.
- Zeros at frequencies $\omega = 2\pi n/T$, where $n \in \mathbb{N}$.

As with laser phase noise, minimizing seismic noise is crucial for achieving high sensitivities in atom interferometers. This often involves a combination of passive and active vibration isolation techniques, particularly for the retro-reflecting mirror. Understanding the vibration transfer function allows for targeted noise reduction strategies, focusing on the most impactful frequency ranges for a given interferometer geometry. In the next sections, we will present methods to decrease phase noises in our system.

3.2 Laser Phase Noise Considerations

As described in Sec. 3.1.1, the phase stability of the Raman lasers is crucial for achieving high-precision measurements in atom interferometry. Several sources contribute to the overall laser phase noise, each requiring careful consideration and mitigation. In this section, we discuss the main contributors to laser phase noise and our approaches to minimizing their impact.

3.2.1 Reference Oscillator and Microwave Frequency Synthesis

For our scheme of Raman interactions on the ^{87}Rb atom (Sec. 2.2), the two light fields need to have a frequency difference exactly as the hyper-fine splitting of the ^{87}Rb atom. This is equal to $\Delta_{HFS} = 6.834\,\text{GHz}$, meaning it is in the microwave (MW) domain. To ensure that this separation exists, a highly precise MW synthesizer must be used.

There are different methods to generate the two Raman laser fields, such as phase locking a slave laser to a master laser with a frequency offset of Δ_{HFS} like in [66, 68, 69, 71]. Otherwise, one can use the same laser source to create the two light fields using an electro-optical modulator, EOM, as in [48, 51], or an acousto-optical modulator, AOM, as in [72]. In either method, there is a need to use an MW synthesizer to create the frequency offset between the two fields.

Any parasitic noise in the MW signal would be transferred to the laser phase (Sec. 3.1.1), hence the need for a very precise and stable source. The stability is usually achieved by the use of a stable reference oscillator. These devices usually have an output frequency signal of 10 MHz or 100 MHz, necessitating frequency multiplication to fit the MW signal. We use SRS[1] FS725 Rubidium frequency standard in our setup, which has ultra-low phase noise and proved to perform better than our alternative from Accubeat[2] (Fig. 12).

We opted to use the single source and EOM method (Sec. 4.2.2), as this has multiple advantages that will be described in the next sections. For the MW synthesizer, we use the SRS SG384 signal generator. Fig. 13 shows its performance relative to two other signal generators (Rohde-Schwartz[3] SMR 20 and Windfreak[4] SynthHD PRO) which we have in our lab.

3.2.2 Laser Phase Lock

The phase coherence between the two Raman laser fields is achieved by using a phase-locked loop (PLL). This is essential when two different laser sources are used, as each source will have its own phase. However, even when using only one source to create the two Raman beams, they will, in most cases, need to be separated and recombined (as in [51, 72]) and the difference in the optical paths will create phase differences. The PLL, similar to the creation of the frequency offset between the Raman beams, uses a reference signal for the electrical mixer from the reference oscillator.

[1] www.thinksrs.com
[2] www.accubeat.com
[3] www.rohde-schwarz.com
[4] windfreaktech.com

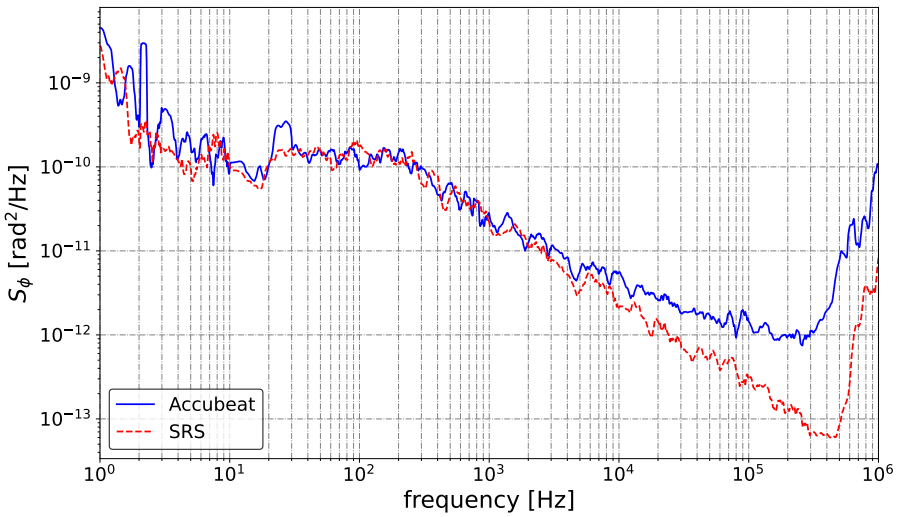

Figure 12: Reference clock noise measurements: Phase noise power spectral density (PSD) measurements of Rubidium frequency standards available in our lab. Measurements were performed for a center frequency of 10 MHz.

As we utilize a single laser source, our PLL system is necessary only to compensate for the differences in the optical paths. Hence, the optical signals are measured as close as possible to where they are combined, as presented in Fig. 21. The Vescent[5] D2-135 system is employed for the PLL. This system promises high performance and ease of use, but due to ongoing technical challenges, its full characterization in our system remains to be completed.

3.2.3 Laser Intensity Fluctuations

Intensity fluctuations in the Raman lasers can significantly impact the performance of the atom interferometer through several mechanisms. As described by Le Gouët et al. [68], these fluctuations contribute to the interferometer phase noise in multiple ways:

- **Rabi Frequency Fluctuations:** The effective Rabi frequency Ω_R of the Raman transition depends on the product of the two laser field amplitudes (Sec. 2.2). Intensity fluctuations, therefore, lead to variations in the Rabi frequency, affecting the population transfer efficiency during the interferometer pulses (Sec. 2.3). It can be quantified by the variance of the atomic population inversion [73]: $\sigma_W = \sqrt{3}\pi\sigma_I/2I$, where σ_I is the variance in the total Raman beams' intensity, I.

- **AC Stark Shift:** Variations in laser intensity lead to fluctuations in the AC Stark shift [74], which directly affects the energy levels of the atoms. This one-photon light shift can be expressed as a linear combination of the laser intensities, $\delta\nu = \beta_1 I_1 + \beta_2 I_2$. Here β_1 and β_2 are the AC Stark shift coefficients for the two Raman lasers, I_1 and I_2 are their respective intensities. These shifts can be mitigated by adjusting the intensity ratio between the two laser fields to $\beta_1 I_1 + \beta_2 I_2 = 0$. Still, intensity fluctuations occurring on times scales shorter than the interferometer duration can lead

[5] vescent.com

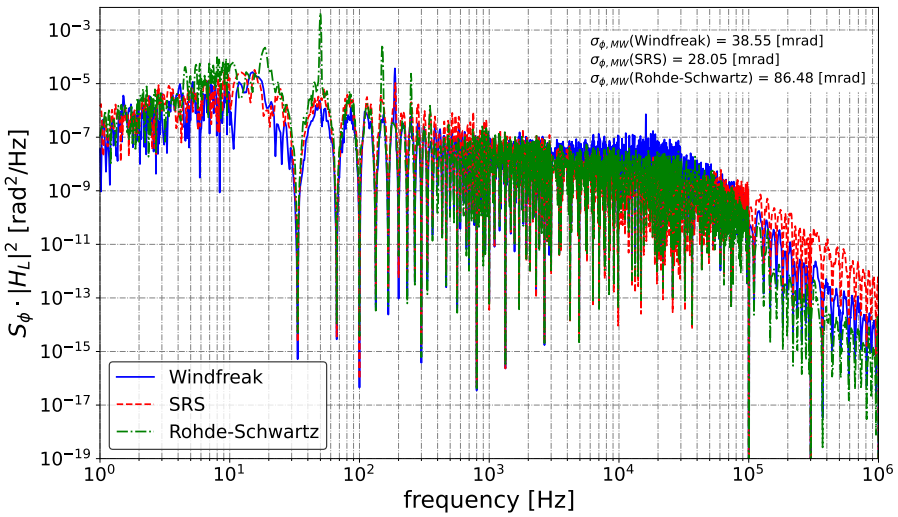

Figure 13: Microwave synthesizers noise measurements: Microwave synthesizers phase noise power spectral density (PSD), calculated by multiplying the PSD measurement of each device with the laser phase transfer function $H_L(2\pi f)$ from Sec. 3.1.1. The measurements have been done for a center frequency of $\Delta_{HFS} = 6.834\,\text{GHz}$. The interferometer phase noise $\sigma_{\phi,\text{MW}}$ is calculated from the data using numerical integration.

to noise in the interferometer phase.

- **Two-Photon Light Shift:** In addition to the AC Stark shift, there is also a two-photon light shift that depends on the intensities of both Raman beams. This shift can be expressed as, $\Omega_R^2\,(1/\Delta_1 + 1/\Delta_2)$, where Δ_1 and Δ_2 are the detunings from the intermediate state for the two Raman transitions.

Several methods have been demonstrated to mitigate these effects, such as active intensity stabilization, adjustment of the intensity ratio between the two Raman beams and use of composite pulse sequences. In our system, we planned to implement active intensity stabilization and adjustment of the intensity ratio by controlling the intensity of one of the Raman beams relative to the other, using an acousto-optical modulator (AOM5 in Fig. 21) and a feedback loop from the signal of the beat note photodiode.

3.2.4 Laser Source Phase Fluctuations

The intrinsic phase noise of the laser sources themselves is another important consideration in atom interferometry. This noise arises from various physical processes within the laser cavity and can significantly impact the overall phase stability of the Raman beams.

The phase noise of a laser is typically characterized by its frequency noise PSD or phase noise PSD. For many lasers, the frequency noise PSD follows a characteristic shape, with higher noise at lower frequencies (often with a $1/f$ dependence) and a white noise floor at higher frequencies.

To minimize the impact of laser source phase fluctuations, several strategies can be employed:

- Use of low-noise current drivers and temperature controllers to reduce technical noise sources.

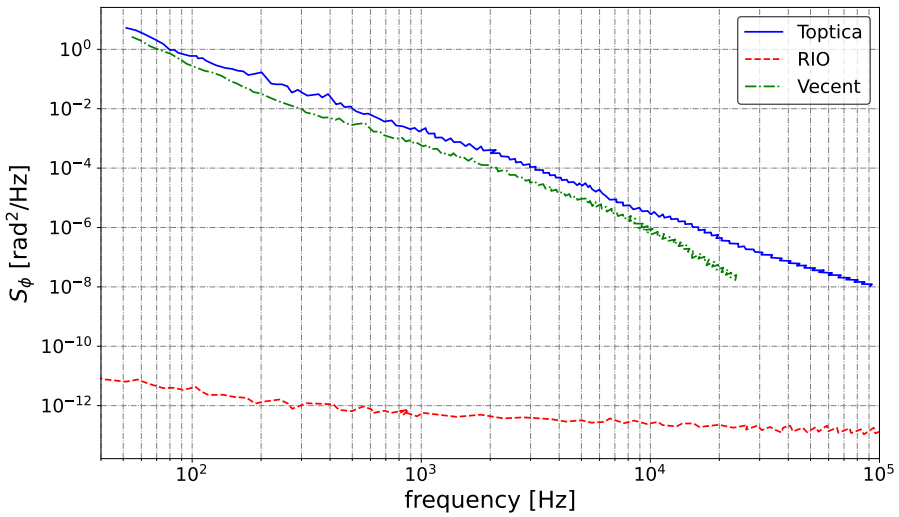

Figure 14: Laser phase noise comparison: Lasers phase noise power spectral density (PSD), taken from the companies' data sheets: Toptica DL Pro ECDL, Vescent DBR and RIO GRANDE.

- Implementation of active frequency stabilization techniques, such as locking to a high-finesse optical cavity or an atomic transition.
- Use of low-noise laser technologies such as fiber lasers or solid-state lasers, although these often require frequency doubling to reach the wavelengths used for Raman transitions in alkali atoms.

We opted for the last option and implemented a telecom fiber laser (RIO GRANDE[6]), as described in Sec. 4.2.2. This laser allows for significantly lower phase noise relative to the external cavity diode lasers (ECDL), like Toptica[7] DL Pro, and distributed Bragg reflector (DBR), from Vescent, which we had available in the lab. Fig. 14 shows a comparison between the different lasers in our lab.

3.3 Vibration Cancellation Methods

Vibration noise is a significant limiting factor in the sensitivity of atom interferometers, particularly for precision measurements such as those in gravimetry and inertial sensing. To address this issue, we implemented and explored a variety of vibration cancellation methods.

3.3.1 Passive Isolation

Passive isolation methods utilize mechanical systems to attenuate vibrations without requiring external power or control systems. Our primary approach to vibration reduction involves a multi-stage passive isolation system:

1. **Optical Table:** The experimental apparatus is built on an optical table (CleanTop 784 of TMC[8]) equipped with pneumatic piston legs (Micro-g series). This provides basic vibration filtering through

[6] rio-lasers.com
[7] www.toptica.com
[8] www.techmfg.com

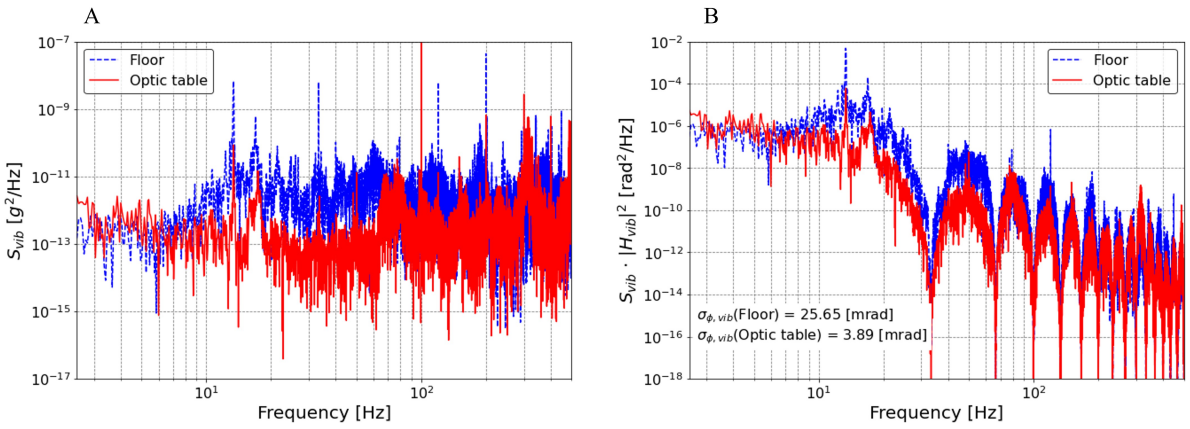

Figure 15: Vibration noise measurements in the lab: The red full line represents the measurements on top of the optic table, while the dashed blue line shows the measurements on the floor. (A) Plot of the vibration noise power spectral density (PSD) taken with a Wilcoxon 731A accelerometer. (B) Vibration phase noise PSD, calculated by multiplying the PSD measurement of (A) with the vibration transfer function of Eq. 58. The interferometer phase noise $\sigma_{\phi,"vib"}$ is calculated from the data using Eq. 54.

the following mechanism:

- The pneumatic pistons act as soft springs, creating a low-resonance frequency system.
- Vibrations at frequencies above this resonance are attenuated, as the table's large mass resists rapid movements.
- This system reduces the phase noise from about 25 mrad (measured on the lab floor) to approximately 4 mrad, as can be seen in Fig. 15.

2. **Low-Frequency Isolation Stage:** To further reduce vibrations, we employ a low-frequency negative-stiffness isolation stage (LC-4U from Minus K[9]) placed on top of the optical table. This creates a multi-stage isolation system that significantly improves vibration suppression through:
   - Negative-stiffness mechanisms that cancel the positive stiffness of supporting springs, resulting in a very low natural frequency.
   - Vertical and horizontal vibration isolation, providing comprehensive protection against multi-directional disturbances.
   - No requirement for air or electricity, ensuring consistent performance and minimal maintenance.

The combination of these passive isolation techniques reduces the vibration-induced phase noise to about 0.5 mrad (Fig. 16), a significant improvement over the noise level without the isolation stage.

[9] www.minusk.com

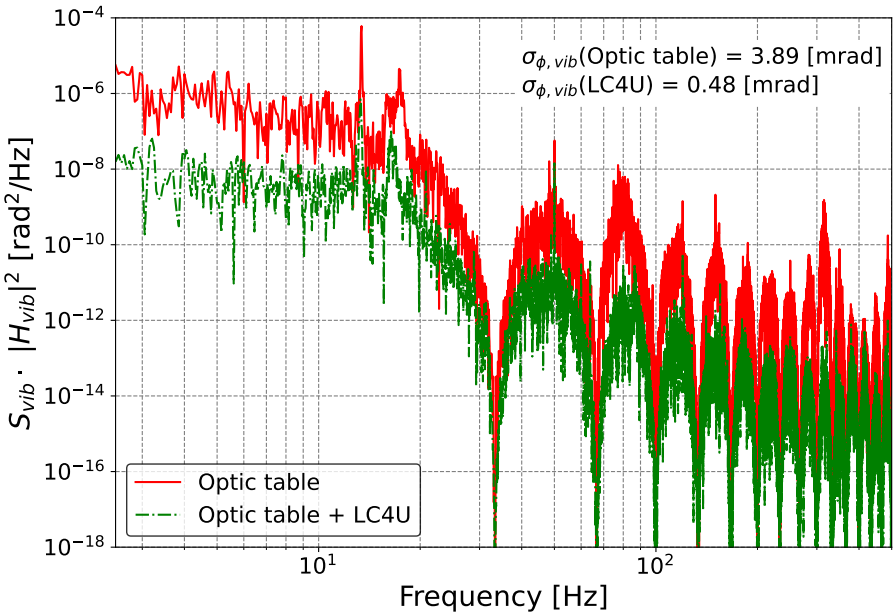

Figure 16: Vibration noise measurements in the lab: Plot of the vibration phase noise power spectral density (PSD) as in Fig. 15. The red full line represents the phase without the LC-4U stage, while the dashed green line shows the results with the stage.

3.3.2 Post-Processing Correction

In addition to passive isolation, we implement a post-processing correction method:

- A high-resolution, ultra-low-frequency accelerometer (Wilcoxon 731A[10]) is installed on the isolation stage, adjacent to the retro-reflecting mirror.
- This accelerometer measures the mirror's vibrations throughout the interferometer sequence.
- The recorded vibration data is then used in post-processing to remove the unwanted interferometer phase caused by these vibrations.

The basic mechanism of this method is as follows: The accelerometer provides a time-resolved measurement of the mirror's motion. Using the known transfer function of the interferometer (Eq. 58), we can calculate how these vibrations affected the interferometer phase (Eq. 54). This calculated phase shift is then subtracted from the measured interferometer phase, effectively cancelling out the vibration-induced errors. This technique allows us to further reduce the impact of residual vibrations not completely eliminated by the passive isolation system.

3.3.3 Performance Evaluation

To evaluate the performance of our vibration cancellation methods, we conducted vibration noise measurements in our lab using the Wilcoxon 731A accelerometer. The vibration phase was calculated numerically using the vibration transfer function (Eq. 58). Figs. 15 and 16 show the measured vibration

[10] wilcoxon.com

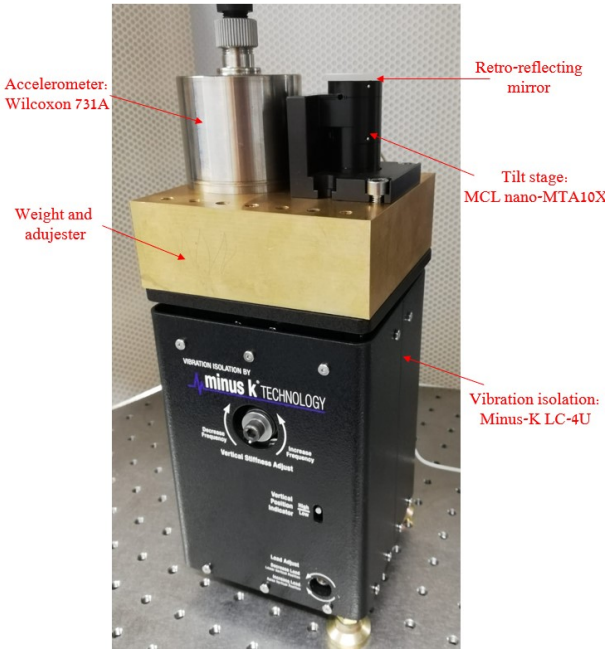

Figure 17: Vibration isolation system: Image of the vibration isolation system, showing the accelerometer and mirror (mounted with a tilt stage) connected to the LC-4U stage via a brass weight. The LC-4U stage is positioned on top of the optical table to provide multi-stage vibration isolation.

noise PSD and the corresponding phase noise PSD for different isolation configurations. These measurements demonstrate that the passive isolation techniques enable us to achieve sub-mrad vibration phase noise, which can be lowered even further by the post-processing technique. This is crucial for high-precision atom interferometry experiments.

While our current vibration cancellation system (Fig. 17) has significantly improved the interferometer's performance, there is still room for further enhancement. Potential future improvements include the implementation of active vibration isolation systems, which use sensors and actuators to dynamically counteract detected vibrations. This can allow the development of real-time vibration compensation techniques, where vibration measurements are used to adjust the interferometer in real time rather than in post-processing. These advancements have the potential to further reduce vibration-induced noise, pushing the boundaries of precision in atom interferometry measurements. However, all these improvements are relevant only if we upgrade our MW synthesizer, as the current device causes phase noise of about two orders of magnitude higher than the seismic noise with our passive isolation system (see Fig. 13 and 16).

4 Experimental Setup

To implement and study the Point Source Interferometer (PSI) technique for high-precision rotation sensing, we designed and constructed a comprehensive experimental apparatus. This section details the key components of our setup, including the vacuum system, laser systems, and magnetic field generation.

The experimental system has evolved significantly from its initial conception. Originally, we began with an apparatus designed for different experiments (like [75]). However, we later decided to build a dedicated PSI setup based on a two-chamber vacuum system: a 2D magneto-optical trap (MOT) chamber and a 3D-MOT and interferometer chamber. This design aims to achieve versatility in creating cold and dense atomic clouds while incorporating all the necessary optical and magnetic fields required for a PSI experiment.

4.1 Overview of the Apparatus

The core of our apparatus consists of two main vacuum chambers: a two-dimensional magneto-optical trap (2D-MOT) chamber and a three-dimensional MOT (3D-MOT) chamber that also serves as the interferometry region. This two-chamber design allows for efficient generation of a cold atom source and subsequent manipulation for interferometry. Fig. 18 illustrates the overall layout of the experimental setup.

The 2D-MOT chamber functions as a source of cold ^{87}Rb atoms, producing a beam of slow atoms directed toward the 3D-MOT chamber. We implement a 2D-MOT+ configuration [76], which includes additional pushing and retarding beams along the atomic beam axis, allowing for enhanced flux and better control over the longitudinal velocity of the atoms.

The 3D-MOT chamber serves a dual purpose. Initially, it captures and further cools the atoms from the 2D-MOT beam. Subsequently, it acts as the interferometry region where the PSI sequence is performed. This chamber incorporates several key components:

- A 3D-MOT setup for atom trapping and cooling.
- High-gradient magnetic coils for enhanced atom confinement.
- Optical molasses configuration for sub-Doppler cooling.
- Raman beams for coherent manipulation of the atomic states.
- Imaging system for detection and analysis of the interference fringes.

A unique feature of our apparatus is the integration of high-gradient magnetic coils inside the 3D-MOT vacuum chamber. This design allows for strong atom confinement while minimizing power consumption and heat generation, enabling a well-localized cold atom cloud for the PSI experiment.

The entire setup is controlled by a comprehensive laser system, providing the necessary frequencies for cooling, trapping, and coherent manipulation of the atoms. Precision magnetic field control and careful design of the optical paths ensure the requisite stability and coherence for high-sensitivity interferometry.

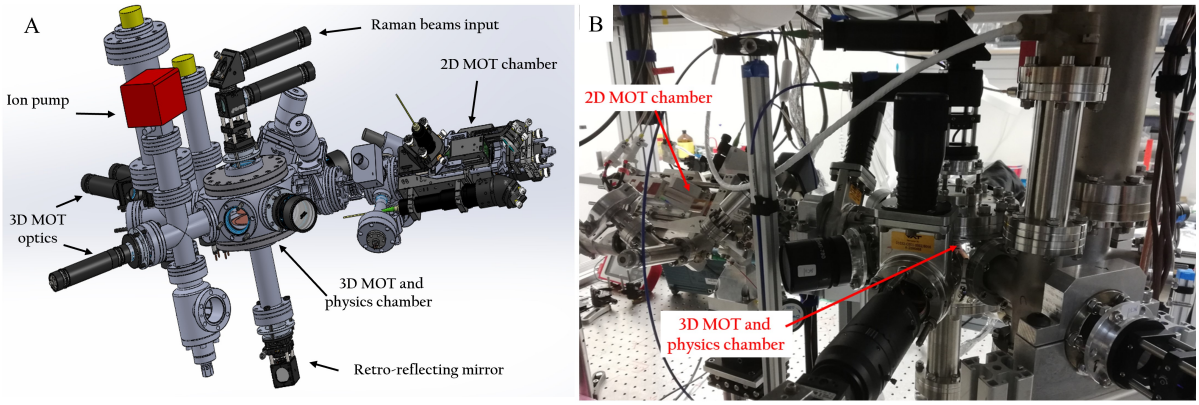

Figure 18: Model and photograph of the experimental apparatus: (A) SolidWorks (SW) model depicts the experimental vacuum system with mounted optics. The right side shows the 2D-MOT, which includes optical elements receiving light from polarization-maintaining (PM) fibers. The 2D-MOT system cools atoms in two axes, while at the third axis, atoms are pushed by another laser beam and reach the 3D-MOT chamber, which is located on the left side of the picture. The 3D-MOT vacuum chamber includes optics designated for the 3D-MOT configuration, optical molasses, optical pumping, the imaging system, and the Raman beams. (B) A picture of the experimental system is provided. On the left is the 2D-MOT vacuum system, which supplies the cold-atom flux to the 3D-MOT located on the right of the picture.

Having outlined the overall structure of our apparatus, we now turn to a detailed description of its key components, beginning with the laser systems that form the heart of our experimental setup.

4.2 Laser Systems

Our experiment requires precise control of laser frequencies and powers to manipulate ^{87}Rb atoms for cooling, trapping, and interferometry (Fig. 19). We employ two main laser systems: two distributed Bragg reflector (DBR) lasers for the MOT operations and a telecom laser for Raman transitions.

4.2.1 MOT Lasers

A MOT system is based on two light fields, usually called "Cooler" and "Repumper". The Cooler beam is tuned slightly below the resonant frequency of an atomic transition, exerting a force on the atoms that reduces their velocity. The Repumper beam, on the other hand, counteracts the depletion of the ground state population caused by the cooling process, ensuring a continuous cycle of absorption and emission of photons, thereby maintaining cooling efficiency. Together, these beams create optical molasses, slowing down atoms and trapping them at the center of the magnetic field gradient.

Two DBR laser diodes (Vescent D2-100-DBR) form the core of our MOT laser system, as presented in Fig. 20. Each diode provides an output power of approximately 200 mW at 780 nm. The first DBR laser (Repumper) generates both the repumping and optical pumping frequencies. It is precisely tuned to the D2-line $|F = 1\rangle \rightarrow |F' = 1\rangle$ transition and is stabilized using an error signal obtained through polarization spectroscopy, with the assistance of a Vescent D2-125 servo. The second DBR laser (Cooler)

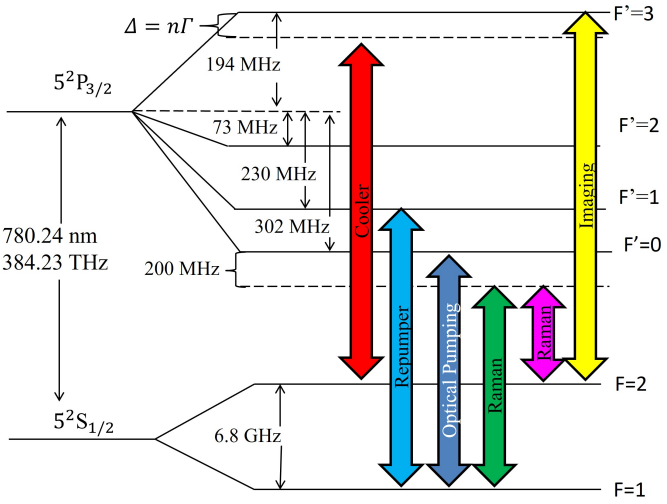

Figure 19: Laser frequencies used in the experiment: Not-to-scale diagram of the ^{87}Rb D_2 transition hyperfine structure [77], with the necessary laser frequencies for the experiment presented. The Cooler laser is detuned by $\Delta = n\Gamma$, where $\Gamma \simeq 2\pi \cdot 6\,\text{MHz}$ is the linewidth of the $5^2\text{P}_{3/2}$ level, from the $F' = 3$ hyperfine level. The Raman lasers are precisely detuned by the hyperfine separation of the ^{87}Rb, $\Delta_{HFS} = 6.834\,\text{GHz}$ from each other, and are red detuned by 200 MHz from the $5^2\text{P}_{3/2}$ manifold.

is used for generating the cooling frequency. It is tuned slightly below the D2-line $|F = 2\rangle \rightarrow |F' = 3\rangle$ transition of ^{87}Rb. This laser is phase-locked to the second DBR laser using a phase-lock loop system implemented with a Vescent D2-135 module. This approach allows a temporal tuning of the frequency of the Cooler laser relative to the locked Repumper laser, without the need of extra electro-optic devices, for the different stages of cooling, like optical molasses. To meet the total power requirements for cooling, we use a tapered amplifier (TA, TPA780P20 by Thorlabs[11])) to boost this laser's output. This amplification results in a total power of approximately 2 W.

The Cooler laser is split and coupled into five polarization-maintaining (PM) fibers for various functions in the 2D and 3D-MOT systems, to be described more thoroughly in Sec. 4.4. Meanwhile, the Repumper laser is co-injected into three of these fibers (Fig. 20). As the cooling stage is only necessary for the preparation of the atomic cloud for the PSI experiment, we use mechanical shutters to stop the lasers from reaching the system when they are not required.

As specified, the Repumper laser is also used for the preparation of the initial quantum state of the atoms in the experiment by optical pumping. For this goal, we use an acousto-optic modulator (AOM) to downshift its frequency by 72 MHz, tuning the beam to the D2-line $|F = 1\rangle \rightarrow |F' = 0\rangle$ transition. The AOM is also used as a fast shutter of the light field.

[11] www.thorlabs.com

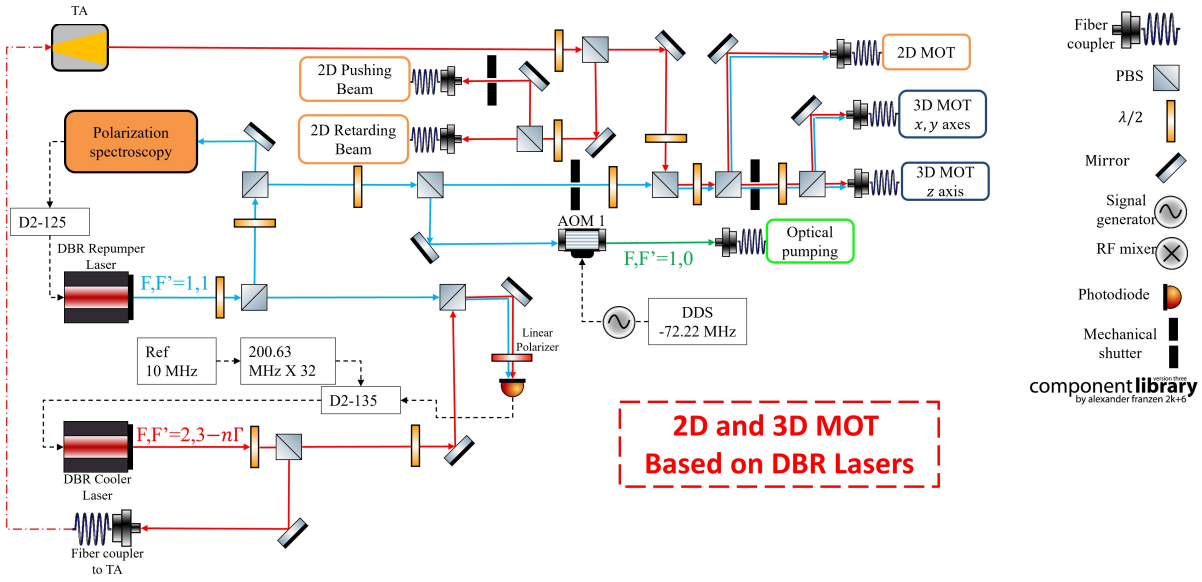

Figure 20: Schematic of the MOT lasers system: The system consists of two DBR lasers (D2-100-DBR by Vescent) primarily used to provide the 2D and 3D-MOT Cooler (red) and Repumper (blue) beams. The optical pumping beam is split from the locked Repumper laser, passing through an acousto-optical modulator (AOM), which downshifts its frequency to the D2-line $|F = 1\rangle \rightarrow |F' = 0\rangle$ transition. The Cooler, locked by a phase-lock on the Repumper laser, then passes through a tapered amplifier (TA). It is then coupled to five PM fibers for various functions in the 2D and 3D-MOT systems.

4.2.2 Raman Laser System

For the stimulated Raman transitions required in the interferometer sequence, we employ a narrow linewidth communication laser (RIO GRANDE[12]) operating at 1560 nm. This choice is motivated by the need for low phase noise in the interferometric signal (Sec. 3.1.1). The 1560 nm output is frequency-doubled to 780 nm using a high-stability bow-tie power enhancement cavity for critical second harmonic generation (SHG) from Agile Optics[13]. This configuration provides a 780 nm beam with a total power of up to 1 W and an estimated linewidth of approximately 20 kHz.

We lock this laser to the D2-line $|F = 2\rangle \rightarrow |F' = 1 - 3\text{CO}\rangle$ transition (where CO refers to a crossover transition) using FM spectroscopy. The error signal is processed using a lock-in amplifier, and the locking is achieved through a home-built proportional-integral-derivative (PID) controller.

The Raman laser system is configured to produce a Λ configuration (Sec.,2.2). This configuration consists of two phase-coherent beams with a frequency separation matching the ^{87}Rb ground state hyperfine splitting (approximately 6.834 GHz). Both beams are red-detuned by 200 MHz from the $5^2P_{3/2}$ manifold, as illustrated in Fig. 21. This is achieved through the use of acousto-optic modulators (AOMs) and an electro-optic modulator (EOM). The EOM plays a critical role in creating hyperfine splitting between the two beams. The EOM generates frequency sidebands based on its microwave (MW) driving frequency. To suppress unwanted frequencies, we employ injection-locking to a slave laser. This slave

[12] rio-lasers.com
[13] www.agile-optic.com

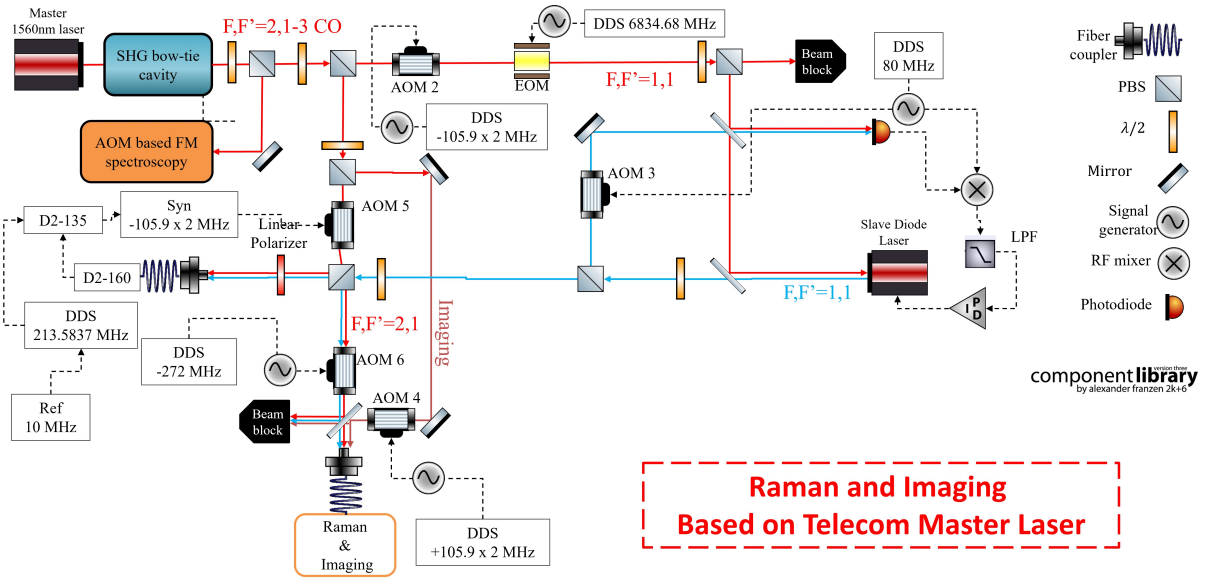

Figure 21: Schematic of the Raman laser system: The 1560 nm output is frequency-doubled and then split into two Raman beams and an imaging beam. The first Raman beam passes through an AOM and EOM for frequency control and is then injected into a slave laser for sideband filtering and power amplification. The second Raman beam is frequency-shifted and phase-controlled by another AOM. Both beams are then combined and coupled into a polarization-maintaining (PM) fiber for delivery to the 3D-MOT chamber. A portion of each beam is used for phase-locking to minimize interferometer phase noise.

laser is tuned to have its gain resonance at the desired frequency, which in our scheme corresponds to the D2-line $|F = 1\rangle \rightarrow |F' = 1\rangle$ transition. We use a control loop to ensure the stability of the gain resonance frequency by controlling the slave-laser's diode current. The injection locking serves a dual purpose. Firstly, it suppresses the unwanted frequencies created by the EOM through a coherent process. Secondly, it acts as an amplifier. An input of 10 μW results in a total output power of approximately 150 mW.

The output laser from the injected slave is then combined with the second Raman beam at a frequency that matches the D2-line $|F = 2\rangle \rightarrow |F' = 1\rangle$ transition. This is achieved via a polarized beam splitter (PBS). A small portion of these beams is taken for a phase-lock loop (PLL), using a Vescent D2-135 system and an AOM to correct the phase of the second Raman beam (depicted as AOM 5 in Fig. 21). The rest of the beams power is passed through another AOM (depicted as AOM 6 in Fig. 21), which downshifts the Raman lasers frequencies to be red-detuned from the $5^2P_{3/2}$ manifold, and then injected into a PM fiber. The AOM is also used as a fast shutter to control the duration of the Raman pulses for the interferometer sequence (Sec. 2.3).

The doubled telecom laser is also used for the absorption imaging stage, where a small portion of its power is shifted using an AOM to be resonant with the D2-line $|F = 2\rangle \rightarrow |F' = 3\rangle$ transition. It is then combined with the two Raman beams and injected into the same fiber to allow vertical imaging (Sec. 4.4). We also use a scheme where the imaging is injected into a different fiber for side imaging.

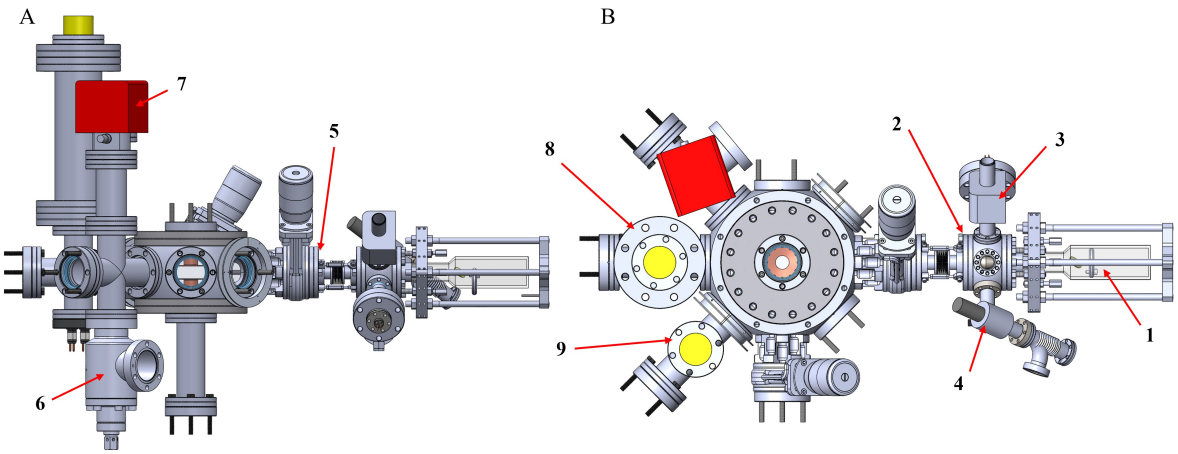

Figure 22: Detailed model of the system without the optics: (A) Side view and (B) a top view. Key components: (1) 2D-MOT glass cell connected to the hexagonal vacuum chamber (2). (3) Ion pump for the 2D-MOT chamber and (4) the isolation valve to connect to a turbo pump station. (5) Port aligner and gate valve that connects between the two chambers. (6) Turbo pump and (7) ion pump of the science chamber. (8) Titanium sublimation pump. (9) Ion gauge.

Having described the laser systems in detail, we now focus on the vacuum infrastructure that provides the ultra-high vacuum environment necessary for our cold atom experiments.

4.3 Vacuum Systems

Our vacuum system consists of two chambers: a 2D-MOT chamber for generating a cold atom flux and a 3D-MOT chamber for atom trapping and interferometry, which also serves as the science chamber. Fig. 22 provides a detailed SolidWorks model of the vacuum system.

4.3.1 2D-MOT chamber

The 2D-MOT system is based on the design by Chaudhuri et al. [76] and includes a rectangular anti-reflective (AR) coated optical glass cell and a metal ultra-high vacuum (UHV) cell. This chamber is connected to a spherical hexagonal vacuum chamber (Kimball Physics[14]) via a CF 40 flange. A Rubidium atom dispenser, an isolation valve, and a vacuum pump are attached to the hexagon using separate CF 16 ports. The 2D-MOT is configured to operate in a 2D-MOT+ mode, which incorporates two counter-propagating laser beams (pushing and retarding) along the third dimension, in addition to the standard cooling and trapping in two dimensions. This configuration, to be elaborated further in Sec. 4.4, enhances the atomic flux and allows better control over the longitudinal velocity of the atoms.

The 2D-MOT chamber has its own vacuum system, including an Agilent[15] VacIon 2 L/s ion pump and the option to connect a turbo pump unit via a CF 16 isolation valve. This ensures that the 2D-MOT vacuum system is completely independent of that used for the 3D MOT in the science chamber.

[14] www.kimballphysics.com
[15] www.agilent.com

The 2D-MOT chamber is connected to the 3D-MOT chamber via a differential pumping tube (DPT), a flexible port aligner, and a gate valve. The DPT enables the transfer of atoms to the 3D-MOT by connecting the two regions, maintaining a pressure differential of about four orders of magnitude. The port aligner and a gate valve allow the isolation of the 2D-MOT chamber from the science vacuum chamber and enable angle adjustments crucial for atomic beam alignment.

The DPT has a small entrance hole diameter of 1.5 mm, which gets larger in eleven steps, with each increasing the diameter by 0.5 mm. This results in an exit hole of 7 mm in diameter. This setup allows can tolerate a high pressure of $10^{-8} - 10^{-7}$ Torr in the 2D-MOT chamber, while achieving a background pressure of $10^{-11} - 10^{-12}$ Torr in the main chamber.

4.3.2 3D-MOT chamber

The 3D-MOT chamber utilizes a Kimball Physics hexagon equipped with eight CF 40 ports and two CF 100 ports. This chamber is designed to capture the atom flux from the 2D-MOT and perform the PSI sequence. It incorporates optics for the MOT, optical molasses, optical pumping, and Raman transitions. The chamber is also connected to standard vacuum instruments such as an ion pump, ion gauge, titanium sublimation pump, and a gate valve.

This chamber is designed to operate at a low pressure of approximately $10^{-11} - 10^{-12}$ Torr, to enable a low probability of background gas collisions to affect the interferometer. We use the 2D-MOT as the atom source instead of the more traditional alkali dispensers. We installed Rb dispensers in the 3D-MOT chamber as a backup in case the 2D-MOT system encounters problems in the future. To achieve the required low UHV regime, we installed a SAES[16] NexTorr D200 pump in the science chamber. This pump combines an ion pump with a non-evaporable getter (NEG) pump, providing efficient pumping for a wide range of gases. When necessary, such as when particles no longer adhere to the surfaces within the vacuum chamber and cause a slight pressure increase, a titanium sublimation pump (TSP) is used. The TSP coats the vacuum surfaces with titanium, which acts as a getter pump by increasing the reactivity and sticking probability of particles to the surfaces, thereby maintaining the UHV conditions. An ion gauge is used to control the vacuum level in the chamber.

This comprehensive vacuum system, combining differential pumping, ion pumps, NEG technology, and titanium sublimation, ensures the ultra-high vacuum conditions necessary for precise atom interferometry experiments. These ultra-high vacuum conditions are crucial for minimizing collisions between the cold atoms and background gas particles, which could disrupt the coherence of the atom interferometer.

4.4 Optical Setup

The optical setup is a crucial component of our experimental apparatus, enabling precise control and manipulation of the atomic ensemble throughout the various stages of the experiment. This section details the optical configurations used in both the 2D-MOT chamber and the science chamber, highlighting how each component contributes to atom cooling, trapping, and interferometry. The careful design of these

[16] www.saesgetters.com

optical systems ensures the efficient atom flux generation, state preparation, and coherent manipulation necessary for high-precision rotation sensing, using the PSI technique.

4.4.1 2D-MOT+ Optics

The 2D-MOT+ configuration [76] is an enhanced version of the standard 2D-MOT, designed to improve atomic flux and provide better control over the longitudinal velocity of the atoms. This setup incorporates cooling and trapping in two dimensions, with additional pushing and retarding beams along the third dimension.

The optical path for the 2D-MOT+ begins with a split polarization-maintaining optical fiber delivering both Cooler and Repumper beams, as described in Sec. 4.2. These beams are then shaped and directed into the vacuum chamber as follows: Component 1 in Fig. 23 refers to this fiber, connected to two collimators on each side of the cell (component 2 in Fig. 23). The collimators create an output wavefront of elliptical cross-section ($3 \times 1\,\mathrm{cm}^2$) and circular polarization via passage through a quarter wave-plate. This shaped beam is sent into the vacuum cell through two non-polarizing beam-splitters (NPBS) and a mirror (component 3 in Fig. 23). This results in approximately homogeneous beam intensity inside the chamber, particularly in the central region of interest. To accomplish the MOT, the circularly polarized beam entering the chamber is reflected by a retro-reflecting prism (component 5 in Fig. 23). Fig. 24 gives a detailed scheme of the optical path.

To achieve a 2D-MOT+ configuration, in addition to the standard 2D-MOT cooling and trapping in two dimensions, we incorporate two counter-propagating laser beams called the pushing and retarding beams along the third dimension. The counter-propagating configuration is achieved by the mirror around the DPT. These beams are red-detuned and have different optical powers. As a result, the atoms are cooled and simultaneously propelled toward the more powerful beam. This allows us to increase the number of atoms in the atomic beam and to control its longitudinal velocity.

The retarding beam is also used as an "optical plug" to prevent atoms from traversing the 2D-MOT chamber and the 3D-MOT chamber after the 3D-MOT loading phase ends. This optical plug is not perfect, but it does significantly lower the atomic flux. A mechanical shutter is then used to prevent the light from the Cooler and Repumper lasers from reaching the 2D-MOT fiber, thereby stopping the MOT process in this chamber. Overall, it ensures that a negligible number of atoms pass between the chambers in the critical stage of the interferometer.

4.4.2 Science Chamber Optics

The science chamber houses multiple optical systems essential for the various stages of our experiment. These include:

- A 3D-MOT setup for further cooling and trapping of atoms from the 2D-MOT.
- Optical molasses beams for sub-Doppler cooling.
- Optical pumping beams for state preparation.

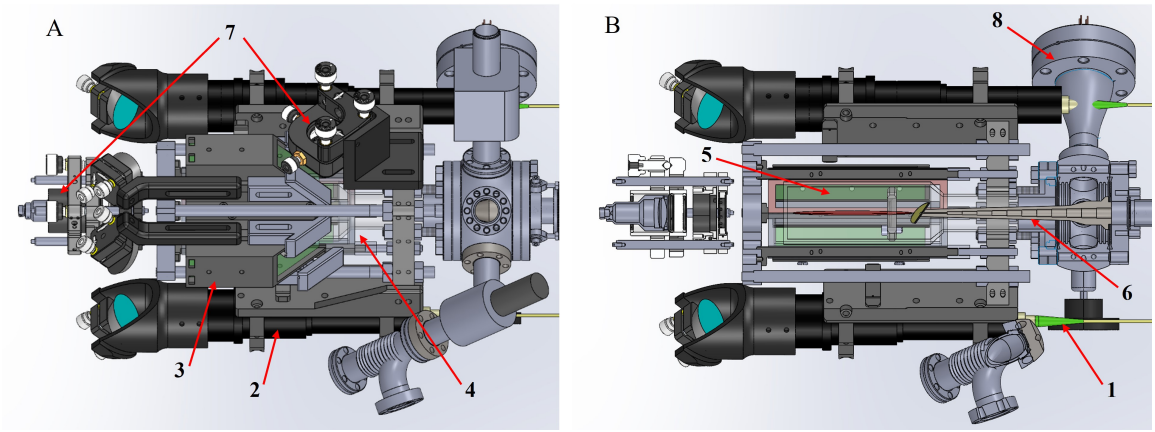

Figure 23: Detailed model of the 2D-MOT system: (A) Top view of the 2D MOT system and (B) a section view from the center of the 2D MOT system. Key components: (1) Optical fiber guides the laser beam from the optical system to the 2D MOT. The beam consists of two wavelengths, for the Cooler and the Repumper. (2) Collimator that creates the needed laser beam polarization and shape. (3) Two non-polarizing beam-splitters (NPBS) and a mirror to guide the beam into the vacuum chamber. (4) The 2D-MOT glass cell. (5) A retro-reflecting prism to reflect the beam after it passes through the cell. (6) The aperture of the differential pumping tube (DPT). A circular mirror is mounted around the DPT to reflect the retarding beam at a 90° angle. (7) Entrance location of the pushing and the retarding beams. (8) The Rb dispenser.

- Raman beams for coherent manipulation in the interferometer sequence.
- Imaging beams for detection.

Each of these systems requires precise alignment and polarization control to achieve the desired manipulation of the atomic ensemble. We will now describe the optical path for each of these systems in detail.

The Raman beams, along with the imaging beam, are delivered to the system through a PM fiber (Fig. 21). A collimator creates an output beam with a diameter of 17 mm. These beams are then combined with the z axis 3D-MOT beam (transferred by a separate PM fiber, Fig. 20) using a 30:70 NPBS. Half waveplates before the NPBS and a quarter waveplate after it ensure the desired polarizations of the beams inside the vacuum chamber. The combined beams pass through the center of the vacuum cell. Upon exiting the chamber, the beams enter another quarter waveplate and a polarization beam splitter (PBS). This arrangement reflects out the imaging beam and one of the Raman beams, while transmitting the MOT beam and the other Raman beam towards a retro-reflecting mirror. This is based on the scheme described in Sec. 2.2.2. The retro-reflecting mirror, mounted on a rotating stage, simulates system rotation without rotating the entire interferometer [78, 79]. After passing through the PBS and the quarter waveplate again, these beams are redirected by the mirror back into the vacuum chamber with the correct polarization. Fig. 25A illustrates the beam paths along this axis.

The remaining two MOT beams complete the standard six-beam MOT configuration. They enter the chamber through CF 40 windows, traverse the chamber center, and exit from opposite windows. Each beam is delivered via a split PM fiber and passes through a collimator with an integrated quarter

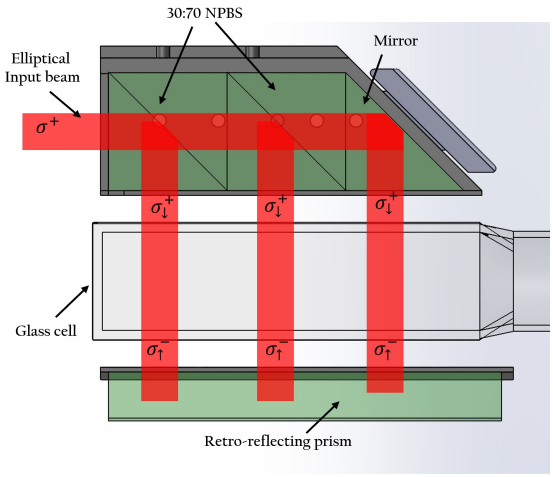

Figure 24: Schematic representation of the optical beam path of the 2D-MOT system: The elliptical ($3 \times 1\,\mathrm{cm}^2$), circularly polarized (σ^+) beam from the collimator (see Fig. 23) is directed into the 2D-MOT's glass cell. To illuminate the entire length of the cell, we pass the beam through two non-polarizing beam-splitters (NPBS), each reflecting some of the power into the cell (splitting ratio of $R = 30\%; T = 70\%$). These are followed by a mirror that fully reflects the remaining power, thus the total power is spread homogeneously over the whole cell. After passing through the cell, the light is retro-reflected from a long prism, which causes the circular polarity of the light to flip from (σ^+) to (σ^-) due to the double reflection through the prism.

waveplate. After it exits the chamber, it passes through another quarter waveplate and is retro-reflected by a mirror. This setup allows the beams to re-enter the chamber with the desired polarization for a MOT.

The optical pumping beam is introduced along one of the MOT beam axes, combined with the MOT beam using a PBS. Fig. 25B illustrates the optical arrangement along the axis containing the optical pumping beam and one MOT beam.

In summary, our optical setup is carefully designed to facilitate all stages of the PSI experiment. The 2D-MOT+ configuration provides a high flux of cold atoms, while the science chamber's optical systems enable precise control and manipulation of the atomic ensemble. This comprehensive optical setup allows us to achieve the ultra-cold temperatures, coherent manipulation, and high-precision measurements necessary for rotation sensing using atom interferometry.

4.5 Magnetic Coils

Our experimental apparatus incorporates several magnetic coil systems, each serving specific functions in the atom trapping, cooling, and manipulation processes. These include coils for the 2D-MOT and 3D-MOT, as well as optical pumping and compensation coils, as shown in Fig. 26.

The 2D-MOT chamber employs a rectangular anti-Helmholtz coil configuration to generate the required quadrupole magnetic field. These coils are wound around a metal frame slightly larger than the glass cell dimensions. The coils produce a two-dimensional magnetic field gradient, with the zero-field line

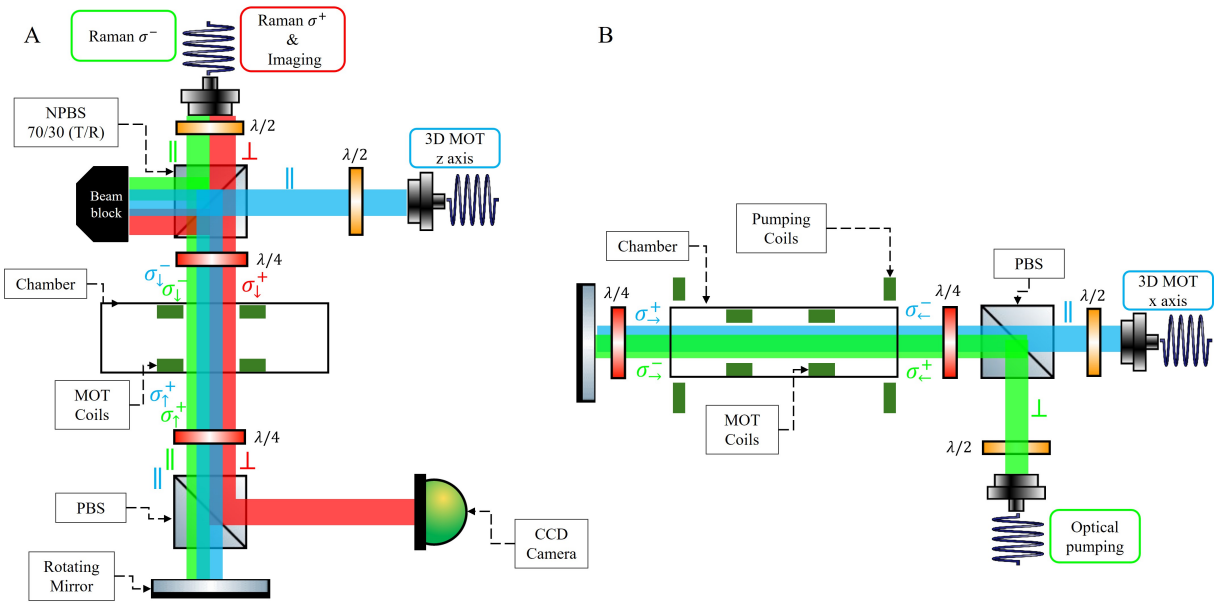

Figure 25: Schematic representation of the optical setup of the science chamber: (A) The optical setup is arranged along the gravity axis. The MOT beam and the Raman beams are combined using a 30:70 non-polarized beam splitter (NPBS) before entering the chamber and the experimental region. The polarization of each beam in the lab reference system, at every position, is indicated in the figure. (B) The optical setup along one of the transverse axes. Here, the MOT beam and the optical pumping beam are combined using a polarized beam splitter (PBS). A similar optical setup is arranged along the other transverse axis to complete the 6-beam MOT, but without the optical pumping beam.

along the atomic beam axis. This configuration is crucial for 2D-MOT operation, as it confines atoms radially while allowing them to propagate along the axis with a near-zero magnetic field, facilitating efficient atom flux generation.

A unique feature of our setup is the integration of high-gradient coils inside the 3D-MOT vacuum chamber. This design, shown in Fig. 27, allows for strong atom confinement while minimizing power consumption and heat generation. The coils are arranged in an anti-Helmholtz configuration and are designed to generate magnetic field gradients of up to 160 G/cm while operating at relatively low currents of 20 A. The coils have an inner diameter of 1.8 mm with a total of 70 loops, resulting in a total resistance of approximately 0.065 Ohm.

These coils are made from UHV-compatible materials, with the coil holders fabricated from oxygen-free copper for optimal heat conduction. We opted for copper due to its non-magnetic properties and high heat conductivity. The contact area between the copper and the chamber is designed to be as large as possible to facilitate heat dissipation. This setup dissipates only 25 W of heat per coil - a significant improvement over conventional setups that typically dissipate 4.8 kW [80].

For the optical pumping, a pair of Helmholtz coils is aligned with the optical pumping beam axis to establish a quantization axis for the atoms during the optical pumping process. These coils generate a uniform magnetic field in the pumping region, ensuring efficient state preparation of the atoms before the interferometry sequence. The uniform field is necessary to define a quantization axis, which allows for

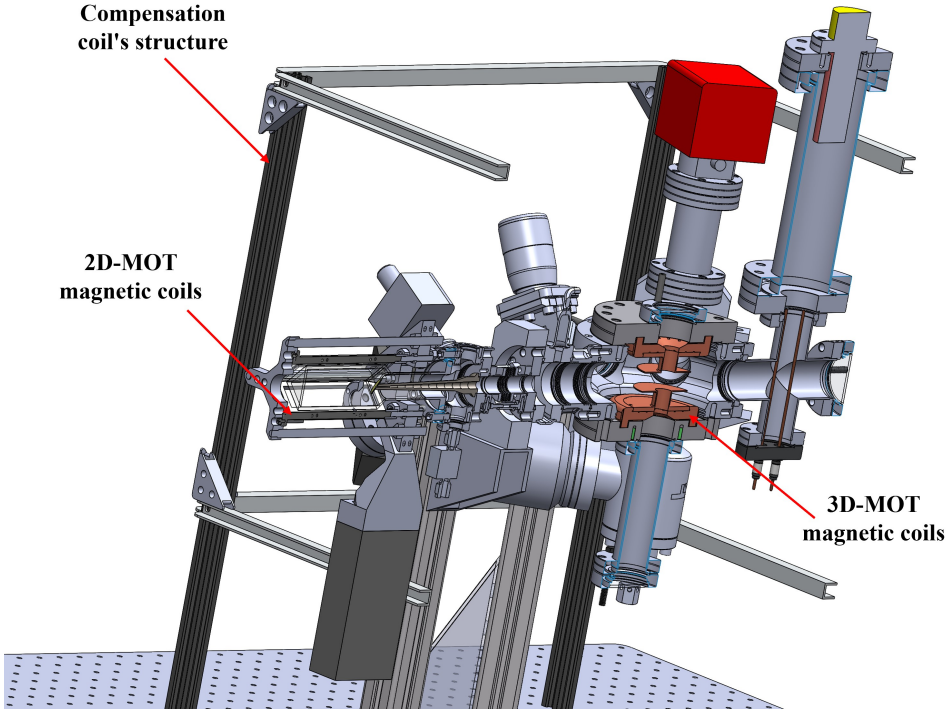

Figure 26: Model of the magnetic coils in the system: A cross-section view at the center of the 3D-MOT and 2D-MOT chambers. The coil structures for the 2D-MOT, the 3D-MOT's high-gradient coils, and the compensation coils, are indicated. The optical pumping coils are not shown in this view.

selective excitation of specific magnetic sublevels, crucial for preparing atoms in the desired initial state of $|F = 1, mF = 0\rangle$ for the interferometer.

Additionally, three pairs of Helmholtz coils are arranged orthogonally around the science chamber to counteract external constant magnetic fields. These compensation coils allow us to cancel out ambient magnetic fields, providing a well-controlled magnetic environment for our atomic ensemble. This is particularly important during the interferometry sequence, where external magnetic fields can introduce unwanted phase shifts and reduce the coherence time of the atomic superposition states.

The careful design and implementation of these magnetic coil systems ensure precise control over the magnetic fields throughout all stages of our experiment, from initial atom trapping to the final interferometry measurements. The combination of external coils for global field control and in-vacuum coils for high gradients provides the versatility and precision required for our atom interferometry experiments.

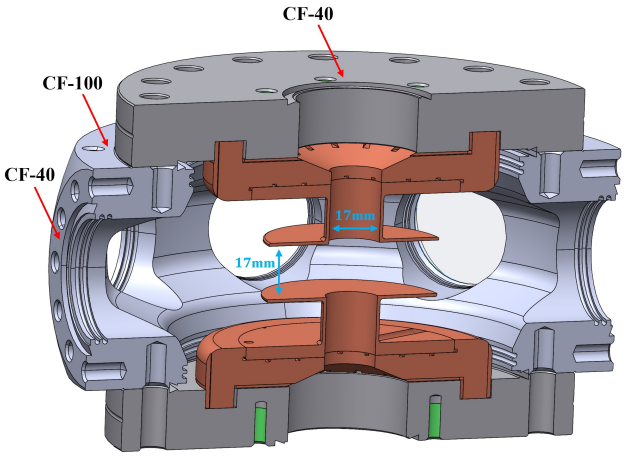

Figure 27: High-gradient coils design: A cross-section view at the center of the 3D-MOT chamber. The bronze-colored structures are the coil holders. Positioned atop the vacuum chamber is a homemade connector CF-100 to CF-40, facilitating connection to the homemade coil holder apparatus. The coils, which have an inner diameter of 1.8 mm, are looped 70 times around the short waist of each coil holder.

5 Squeezed Point Source Interferometer

The point source interferometer (PSI) has proven to be a powerful technique for rotation sensing using cold atoms. Here, we propose a squeezed point-source interferometer (SPSI) to increase the dynamic range of the interferometer and its sensitivity without increasing the operation time or, alternatively, achieving the standard sensitivity with a smaller device. Moreover, a longstanding and sought-after goal is to miniaturize rotation sensing [23, 58, 81, 82], and here we show that the SPSI opens the door to this potential - and even enables a chip-scale device.

To achieve these improvements, we propose a novel approach that manipulates the atomic ensemble's phase-space distribution. Our method is based on adding a stage of pre-acceleration where the initial cloud goes through phase-space squeezing. Phase-space squeezing has been discussed extensively regarding delta-kick cooling [83–87], in which the spread in momentum is decreased at the expense of increasing the spread in position. In contrast, here, we propose to increase the spread in momentum while the spread in position is effectively reduced. As we show, integrating an inhomogeneous repulsive force to accelerate atom motion before the interferometer sequence, can substantially enhance the operational efficiency and sensitivity of a PSI device. We show that the figures of merit are enhanced by several orders of magnitude. Under a definition of compactness, the enhancement in performance is about four orders of magnitude.

An example of the effect of phase-space squeezing on the interferometer is illustrated in Fig. 28. Squeezing leads to both an increase in the number of oscillations within the cloud size and an increase in the contrast.

In the following subsections, we will present a detailed examination of the SPSI method. We begin with an analytical derivation of the key principles and equations governing the SPSI. This is followed by

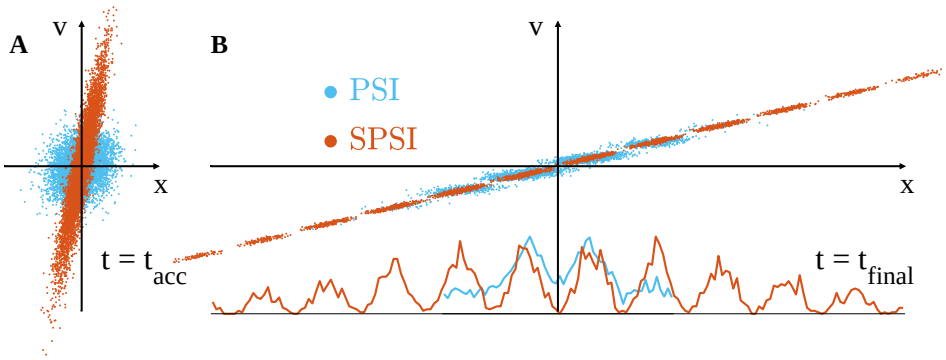

Figure 28: Principle of the squeezing effect in the interferometer: The atomic phase-space distribution is shown for the standard PSI interferometer (blue) and the SPSI interferometer (orange), at two different times: (A) at the start of the interferometer sequence, t_{acc}, occurring just after the acceleration stage due to the repulsive potential pulse, and (B) at the imaging time, t_{final}, following the complete interferometer sequence. The phase space distribution at t_{final} becomes tilted due to expansion, and the velocity-dependent interferometer phase introduces an oscillatory phase-space density upon detecting a single state. As shown at the bottom of (B), the latter oscillation produces a spatial density oscillation, which, upon being projected onto the position axis, forms the observed signal (output) of the interferometer. In the SPSI, when the initial phase-space distribution is squeezed with increased velocity, the subsequent expansion results in a phase-space distribution having a high aspect ratio. Upon projection onto the position axis, the SPSI signal shows improvement with more oscillations and an improved contrast.

a description of our numerical simulations, which provide insights into the behavior of the system under various conditions. Finally, we conduct a comprehensive performance analysis, comparing the SPSI to conventional PSI techniques and exploring its potential for enabling either enhanced performance in standard-size devices or maintaining performance while miniaturizing to a chip-scale device.

5.1 Analytical Derivation

In this subsection, we present the analytical derivation of the SPSI method, beginning with the fundamental principles of the repulsive potential and its effects on atomic motion. Integrating a repulsive potential that varies spatially to accelerate atom motion before the interferometer sequence, can substantially enhance the operational efficiency and sensitivity of a PSI device. Repulsive forces have been discussed in numerous contexts [88–93], but in this context, the repulsive potential serves to enlarge the area enclosed by the interferometer arms while maintaining and even improving the crucial position-velocity correlation. This is achieved by applying a repulsive potential for an acceleration time t_{acc}. Let us define the coordinate system such that the z axis is along the direction of the splitting and recombining laser beam. We may apply a quadratic repulsive potential along one or two axes transverse to z, but for the sake of simplicity, we describe only the dynamics along the x coordinate. If the repulsive potential is quadratic $V_{\mathrm{rep}}(x) = -(1/2)m\omega^2 x^2$, where m is the atomic mass, then after the acceleration stage, the initial coordinates in the direction x of an atom are transformed as

$$x(t_{\mathrm{acc}}) = c_\omega \cdot x(0) + s_\omega \cdot v_x(0)/\omega\,, \quad v_x(t_{\mathrm{acc}}) = \omega s_\omega \cdot x(0) + c_\omega \cdot v_x(0)\,, \tag{59}$$

where $c_\omega = \cosh(\omega t_{\rm acc})$ and $s_\omega = \sinh(\omega t_{\rm acc})$.

In Sec. 5.1.1 we show that the phase-space distribution that forms after the repulsive pulse is exactly equivalent to the distribution that forms after free propagation for an effective duration $t_{\rm eff}$, when the initial distribution is squeezed with effective position uncertainty $\tilde{\sigma}_{x0} = \sigma_{x0}/\eta$ and velocity uncertainty $\tilde{\sigma}_{v0} = \eta\sigma_{v0}$, with the squeezing parameter being

$$\eta \equiv \sqrt{c_\omega^2 + \frac{\omega^2\sigma_{x0}^2}{\sigma_{v0}^2}s_\omega^2}, \tag{60}$$

and the effective time is given by

$$t_{\rm eff} = \frac{s_\omega c_\omega}{\omega\eta^2}\left(1 + \frac{\omega^2\sigma_{x0}^2}{\sigma_{v0}^2}\right). \tag{61}$$

This squeezing parameter η characterizes the degree of phase-space manipulation achieved by the repulsive potential. If $\omega t_{\rm acc} \ll 1$ and $\gamma \equiv \omega\sigma_{x0}/\sigma_{v0} \ll 1$ then $\eta \approx 1$ and $t_{\rm eff} \approx t_{\rm acc}$, such that the acceleration phase is ineffective. Conversely, if $\omega \gg \sigma_{v0}/\sigma_{x0}$ ($\gamma \gg 1$) then even if the acceleration time is not long, such that $\omega t_{\rm acc} \lesssim 1$, then the squeezing parameter is large $\eta \sim \gamma\omega t_{\rm acc}$ and the effective expansion time is $t_{\rm eff} \sim t_{\rm acc}/(\omega t_{\rm acc})^2$. If the acceleration time is long, such that $\omega t_{\rm acc} > 1$ the squeezing becomes exponentially large such that $\eta \approx \sqrt{1+\gamma^2}e^{\omega t_{\rm acc}}$ and $t_{\rm eff} \approx 1/\omega$ is inversely proportional to the repulsive frequency.

We now focus on the practical implementation of the repulsive potential using a blue-detuned laser beam. The repulsive potential can be generated by a laser beam blue-detuned from the atomic resonance by $\Delta > 0$. The effective AC Stark-shift is [74]

$$V_{\rm ac}(\vec{r}) = \hbar\frac{\Omega_R(\vec{r})^2}{4\Delta} = \frac{3\pi\Gamma}{2k_0^3 c}\frac{I(\vec{r})}{\Delta}, \tag{62}$$

where Ω_R is the local Rabi frequency, $k_0 = 2\pi/\lambda_0$ is the optical transition wave-vector, Γ is the spontaneous emission rate, $I(\vec{r})$ is the light intensity, and c is the speed of light. The inverse harmonic repulsive potential could be implemented by the quadratic intensity profile near the center of a Gaussian beam propagating along the z direction. However, a more efficient acceleration may be achieved by designing a fully quadratic beam shape. Here, we consider acceleration in the x direction induced by a laser beam propagating along the y direction and having a homogeneous profile in the z direction in the volume containing the atom cloud. The light beam profile is $I(x,z) = I_0(1 - x^2/x_0^2)$ for $|x| < x_0$, $|z| < z_0/2$ and zero otherwise, where I_0 is the peak intensity and $2x_0z_0$ is the beam cross-section. The peak intensity equals $I_0 = 3P/4x_0z_0$, where P is the beam power, and the potential frequency becomes

$$\omega_{\rm Harmonic} = \sqrt{\frac{9\pi\Gamma P}{4mk_0^3 c\Delta x_0^3 z_0}}. \tag{63}$$

This equation relates the potential frequency to the beam parameters, allowing us to optimize the squeezing effect. The harmonic profile is quite advantageous for achieving a large squeezing factor before the atoms reach the region with a repulsive potential. For example, for the parameters introduced in Fig. 31, $\omega_{\rm Harmonic} = 2\pi \cdot 1220\,{\rm Hz}$.

The optical repulsive potential has the consequent effect of heating the atoms due to scattered photons [74]. Along the direction of beam propagation, the atoms gain momentum in correlation to the

spatial intensity $I(\vec{r})$, which can be compensated by shifting the initial cloud position or, if necessary, by employing a counter-propagating beam. In addition, as will be explained in Sec. 5.1.2, the scattering induces a random walk in velocity space in all directions, potentially enlarging the effective initial cloud size, $\tilde{\sigma}_{x0}$, and consequently decreasing the upper detection limit $\Omega_{\max}$ (Eq. 35). Under the limitations we have taken for the laser power and typical parameter values, this effect reduces $\Omega_{\max}$, e.g., by $\sqrt{2}$ for the parameters of Fig. 31. This effect can be reduced to a negligible level by improving the beam parameters, for example, by equally increasing the beam power P and the detuning Δ. More details about the heating process can be found in Sec. 5.1.2. One could also explore using different types of potential, such as magnetic gradients, to mitigate heating.

5.1.1 Free Evolution of a Gaussian Phase-Space Distribution

To fully understand the SPSI method, it is essential to examine the evolution of the atomic cloud's phase-space distribution. In a two-dimensional phase space of position x and velocity v, a Gaussian distribution in the form of an exponent of a bi-quadratic expression in x and v remains Gaussian in either free evolution or evolution in a quadratic potential. This conservation of the Gaussian form follows from the fact that any linear transformation of a bi-quadratic expression of two variables remains bi-quadratic under such a transformation. Any Gaussian form where the distribution is centered around $x = 0$ and $v = 0$ can be written in the form

$$\rho(x, v, t) \propto e^{-(x-vt)^2/2\sigma_{x0}^2} e^{-v^2/2\sigma_{v0}^2}\,, \tag{64}$$

which is a distribution that evolves under free propagation from an uncorrelated initial distribution at $t = 0$ with a spatial uncertainty σ_{x0} and velocity uncertainty σ_{v0}. This implies that any Gaussian distribution in phase space can be obtained by free propagation over an effective time, t_{eff}, starting from an uncorrelated distribution. This is the way that the effective squeezed distribution with a squeezing factor η is obtained from the distribution that evolves under the repulsive inverse harmonic potential after acceleration over a time t_{acc}. It is easy to acknowledge these properties by noting that a Gaussian distribution in phase space has an elliptical shape in the $x - v$ plane, and any ellipse can be transformed into an ellipse whose axes are aligned along the main axes by a proper rotation transformation.

The quadratic expression in the exponent can also be written in an alternative form that emphasizes the position-velocity correlations in the distribution:

$$\frac{(x-vt)^2}{2\sigma_{x0}^2} + \frac{v^2}{2\sigma_{v0}^2} = \frac{x^2}{2\sigma_f^2} + \frac{(v-x/T)^2}{2\sigma_{vt}^2}\,, \tag{65}$$

where σ_f is the overall spatial width of the cloud, σ_{vt} is the local velocity spread at any given point x and T is an effective time of evolution. The latter three parameters can be expressed in terms of the parameters σ_{x0} and σ_{v0} of the initial uncorrelated distribution and the time of evolution as

$$\sigma_f^2 = \sigma_{x0}^2 + \sigma_{v0}^2 t^2, \qquad \sigma_{vt} = \frac{\sigma_{x0}}{\sigma_f}\sigma_{v0}\,, \qquad T = t\left(1 - \frac{\sigma_{x0}^2}{\sigma_f^2}\right)^{-1}. \tag{66}$$

The expression in Eq. 65 inside the exponent represents a distribution with correlation between position and velocity, such that at a given point x, the width of the velocity distribution is given by σ_{vt}, which

is reduced relative to the initial uncertainty of the velocity by a factor representing the ratio between the initial cloud size and the final cloud size. It is evident that the phase-space volume is conserved during the evolution, as $\sigma_f \sigma_{vt} = \sigma_{x0}\sigma_{v0}$.

If, at a given time, a distribution has the form of Eq. 65, it is possible to express it as a distribution that started at a time t before this time as an uncorrelated distribution of the form of Eq. 64. The variables σ_{x0}, σ_{v0} and t can then be expressed in terms of σ_f, σ_{vt} and T. In particular, we find

$$\sigma_{x0} = \frac{\sigma_{vt} T}{\sqrt{1 + \sigma_{vt}^2 T^2/\sigma_f^2}}\,, \tag{67}$$

and the other two parameters are easily obtained from the latter.

Understanding this free evolution is crucial for the SPSI method, as it allows us to predict and control the atomic cloud's behavior throughout the interferometer sequence.

5.1.2 Effect of Heating

Heating effects are an important consideration in the SPSI method, as they can potentially degrade the squeezing effect and impact the interferometer's performance. Let us consider a situation where an initial uncorrelated distribution has evolved in free space over a time t_{eff} and given rise to a correlated distribution of the form of an exponent of Eq. 65 and then the width of the local velocity distribution σ_{vt} has grown due to quick homogeneous heating. This means that after the heating, the parameters σ_f and T have remained the same as before the heating, while σ_{vt} has grown due to heating. It is now possible to use Eq. 67 for determining the effective initial uncorrelated distribution that would have led by free propagation to the final distribution after heating.

If the heating is very strong, such that after the heating $\sigma_{vt} > \sigma_f$, then the projected initial cloud size at the starting point of the evolution is $\sigma_{x0,\text{eff}} \approx \sigma_f$, and the subsequent evolution of the cloud will be similar to one that starts with the final size upon heating. This means that the heating has erased the position-velocity correlation inside the cloud. Conversely, if the local velocity distribution has not grown considerably during the heating relative to the local velocity uncertainty without heating, then the effect of heating on the consequent evolution is negligible.

In the case of a squeezed phase-space distribution with squeezing factor $\eta \gg 1$ and a cloud size σ_f after the acceleration that is not much larger than the real initial cloud, the local velocity uncertainty is given by $\sigma_{vt} = \eta\sigma_{v0} \cdot (\sigma_{x0}/\eta)/\sigma_f \sim \sigma_{v0}$, which is about the same as the real velocity uncertainty before the squeezing, while the effective initial velocity uncertainty is larger by a factor of η. Let us now assume that after the heating, the local velocity spread grows as $\sigma_{vt} \to \sigma_{vt,\text{tot}} = \sqrt{\sigma_{vt,0}^2 + \sigma_{v,h}^2}$, where $\sigma_{vt,0}$ is the local velocity spread before heating and $\sigma_{v,\text{heat}}$ is the added spread due to heating. Considering the acceleration procedure and taking the free evolution time before heating to be t_{eff} and assuming $\sigma_f \gg \sigma_{x0,\text{eff}}$, the effective initial cloud size projected back after heating becomes

$$\sigma_{x0,\text{eff}}^h \approx \sigma_{vt,\text{tot}} t_{\text{eff}} = \sqrt{\sigma_{x0,0}^2 + \sigma_{v,h}^2 t_{\text{eff}}^2} = \frac{\sigma_{vt,\text{tot}}}{\sigma_{vt,0}} \sigma_{x0,0}\,, \tag{68}$$

where $\sigma_{x0,\text{eff}}^0 = \sigma_{x0}/\eta$ is the initial cloud size without heating and $\sigma_{x0,\text{eff}}^h$ is the projected initial cloud size

after heating. Here, we assumed that the ratio between the local velocity spread after heating and before heating is much smaller than the squeezing factor η.

In summary, our analytical derivation provides a comprehensive framework for understanding the SPSI method. We have shown how the repulsive potential leads to phase-space squeezing, characterized by the squeezing parameter η and effective time t_{eff}. We have also examined the practical implementation using a blue-detuned laser beam and considered the effects of free evolution and heating. These analytical insights provide the basis for our subsequent numerical simulations and performance analysis, which will further demonstrate the advantages of the SPSI method over conventional PSI techniques.

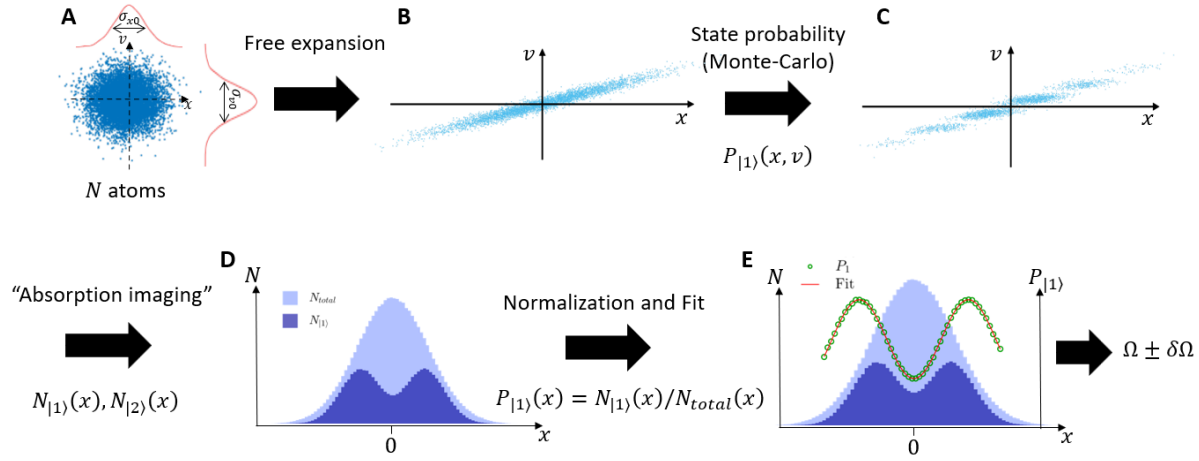

Figure 29: Simulation algorithm flow: Illustration of the key stages in the simulation algorithm. (A) Initialization: N atoms are distributed in a 1D Gaussian distribution with given σ_{x0} and σ_{v0}. (B) Evolution: The atoms' phase-space distribution after free expansion (and repulsive potential for SPSI). (C) State determination: The $|1\rangle$ state distribution calculated using a Monte Carlo method. (D) Imaging simulation: The number of atoms in all states (B) and $|1\rangle$ state (C) projected onto the position axis, simulating absorption imaging. (E) Fringe analysis: Green dots represent the normalized distribution, and the red curve is a sinusoidal fit to these points. From this fit, the angular velocity and its uncertainty are extracted.

5.2 Numerical Simulations

To examine the impact of the SPSI and validate our analytical model, we conduct detailed numerical simulations comparing PSI and SPSI methods. These simulations, implemented in MATLAB, provide insights into the potential performance improvements of our proposed method. We use realistic physical parameters corresponding to existing systems for the cooling, trapping, and light potential phases. The simulation flow, illustrated in Fig. 29, consists of the following key stages:

- Initialization: We generate a cloud of N atoms ($N = 10^6$ in our simulations) following the cooling phase. The atoms are distributed spatially according to a Gaussian distribution with standard deviation σ_{x0} and mean value zero. Their velocities follow a Maxwell-Boltzmann distribution corresponding to the given temperature $\mathcal{T}$. We assume the atoms are optically pumped to the $|F = 1, m_F = 0\rangle$ state of the ^{87}Rb hyperfine manifold (denoted as $|1\rangle$).

- Evolution: For PSI simulations, the cloud undergoes free expansion for the interferometer time $2T_R$, solved using kinematic equations. For SPSI simulations, we first solve ordinary differential equations (ODEs) for the dynamics of each atom under the influence of the light potential. We use MATLAB's 'ode15s' function to solve these $2N$ ODEs for the acceleration time t_{acc}. Following this, we solve the free expansion kinematic equations as in the PSI case.

- State determination: We calculate the probability $P_{|1\rangle}$ for each atom to be in the $|1\rangle$ state based on its final velocity using Eq. 32. We then use a Monte Carlo method to determine the final internal state of each atom.

- Imaging simulation: We simulate a two-state absorption imaging of the atomic cloud by binning the atoms into spatial locations, with each bin representing a "pixel" of the imaging system. We then normalize the counts of atoms in the $|1\rangle$ state to the total population in each bin: $P_1 = N_{|1\rangle}(x)/N_{\text{total}}(x)$. This reveals the interferometer's fringe pattern as per Eq. 30, illustrated in Fig. 30.

- Fringe analysis: We fit a sinusoidal function of the form $y(x) = a\sin(2\pi b \cdot x + c) + d$ to the normalized data. We use a Fast Fourier Transform (FFT) to identify initial guesses for the frequency parameter b, which corresponds to the fringe periodicity k_x. We then use MATLAB's 'fit' function with these initial guesses to find the best fit. From the fitted k_x, we calculate the angular velocity using Eq. 31. The α factor is accounted for by scaling the fit's frequency accordingly before extracting the angular velocity as described in Eq. 30.

- Uncertainty calculation: We compute the uncertainty in angular velocity (single-shot sensitivity $\delta\Omega$) based on the fit uncertainty. We validate this by running multiple simulation repetitions and calculating the standard deviation of the results.

To improve the fit's success rate, we implement a basic image processing stage before normalizing P_1. This involves applying different averaging windows to reduce noise and examining various regions of interest in the image, excluding noisier edges where fewer atoms are counted. Fig. 30 compares the simulation results for both PSI and SPSI methods. It clearly demonstrates the improved contrast and increased number of fringes in the SPSI method, leading to a significantly lower fit deviation and uncertainty compared to the PSI case.

These simulations provide a robust framework for comparing the performance of PSI and SPSI methods under various conditions, allowing us to quantify the improvements in sensitivity and dynamic range offered by our proposed SPSI technique.

5.3 Performance Analysis

Building upon our analytical derivation and numerical simulations, we now present a comprehensive performance analysis of the SPSI method compared to the standard PSI technique. This focuses on three key aspects: sensitivity, dynamic range, and potential for miniaturization.

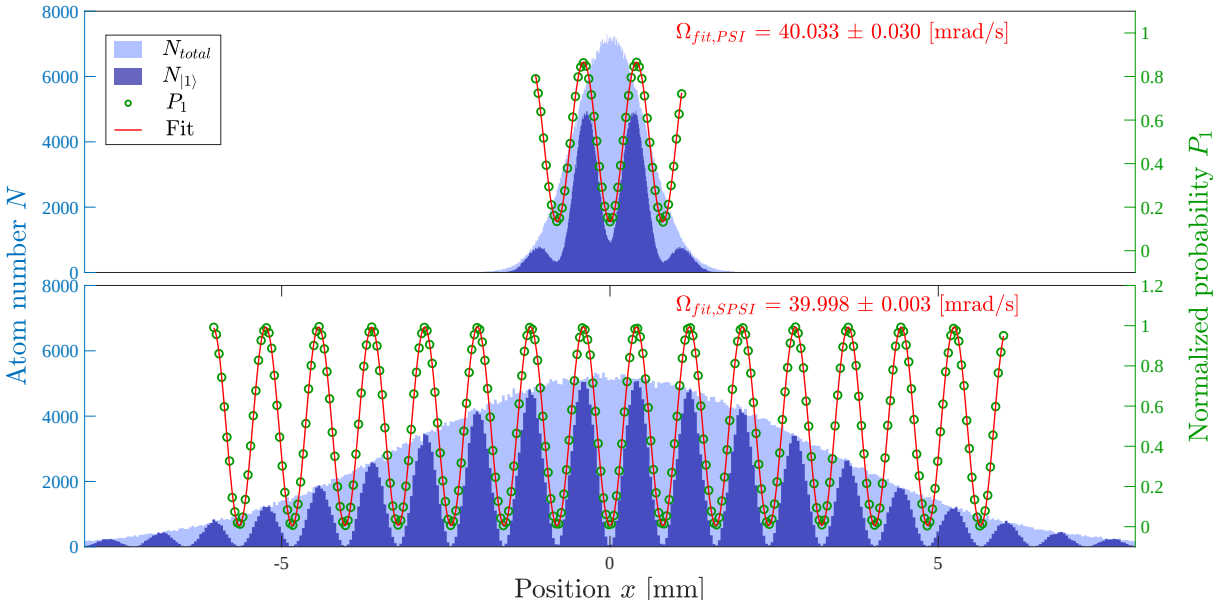

Figure 30: Simulation fringe pattern fit: Comparison of simulation results for PSI (top) and SPSI (bottom) methods. The light blue shaded area shows the total number of atoms in each bin (N_{total}), while the darker shade indicates atoms in the $|1\rangle$ state ($N_{|1\rangle}$). Green points represent the normalized probability for the $|1\rangle$ state ($P_1 = N_{|1\rangle}(x)/N_{\text{total}}(x)$), with the red line showing the sinusoidal fit. Simulation parameters: $N = 10^6$ atoms, $\sigma_{x0} = 100, \mu$m, $\mathcal{T} = 5\,\mu$K, $T_R = 25$ ms, $\Omega = 40$ mrad/s. For SPSI: repulsive potential with $P = 1$ W, beam cross-section $400 \times 400\,\mu\text{m}^2$, $t_{\text{acc}} = 20\,\mu$s, resulting in $\omega = 2\pi \times 1.214$ kHz (Eq. 63), $\eta = 5.4$ (Eq. 60), and $t_{\text{eff}} = 0.84$ ms (Eq. 61). Note the improved contrast and increased number of fringes in SPSI compared to PSI, leading to lower fit deviation and uncertainty.

5.3.1 Sensitivity and Dynamic Range

The sensitivity and dynamic range of the interferometer are crucial performance metrics. Fig. 31 illustrates the contrast of the interference pattern as a function of angular velocity for both PSI and SPSI methods. The SPSI demonstrates a significant improvement in contrast over a wider range of angular velocities, indicating an enhanced dynamic range. We note that at high angular velocities, the fringe spatial frequency increases, making the detection pixel resolution a limiting factor. This causes the numerical contrast to decay more rapidly than the analytical prediction, which does not account for this limitation. Conversely, the SPSI can measure lower angular velocities than PSI due to its larger final cloud radius, which increases sensitivity to slow rotations characterized by low spatial fringe frequencies. This improvement in both limits is depicted in Fig. 31(B) by the analytical curve of the detection range as a function of η according to Eq. 35. Hence, the dynamic range, defined as $\Omega_{\text{max}}/\Omega_{\text{min}}$ (Eq. 35), is improved by a factor of η^2 in the SPSI method. This improvement stems from two effects:

- Reduction of Ω_{min} by a factor of η due to the increased final cloud size: $\sigma_f \approx t_{\text{eff}}\sigma_{v0}\eta$.
- Increase of Ω_{max} by a factor of η due to the reduction of the effective initial cloud radius $\tilde{\sigma}_{x0} = \eta\sigma_{x0}$.

Fig. 32(A) presents a comparison of the relative sensitivity $\delta\Omega/\Omega$ between the two methods. It demon-

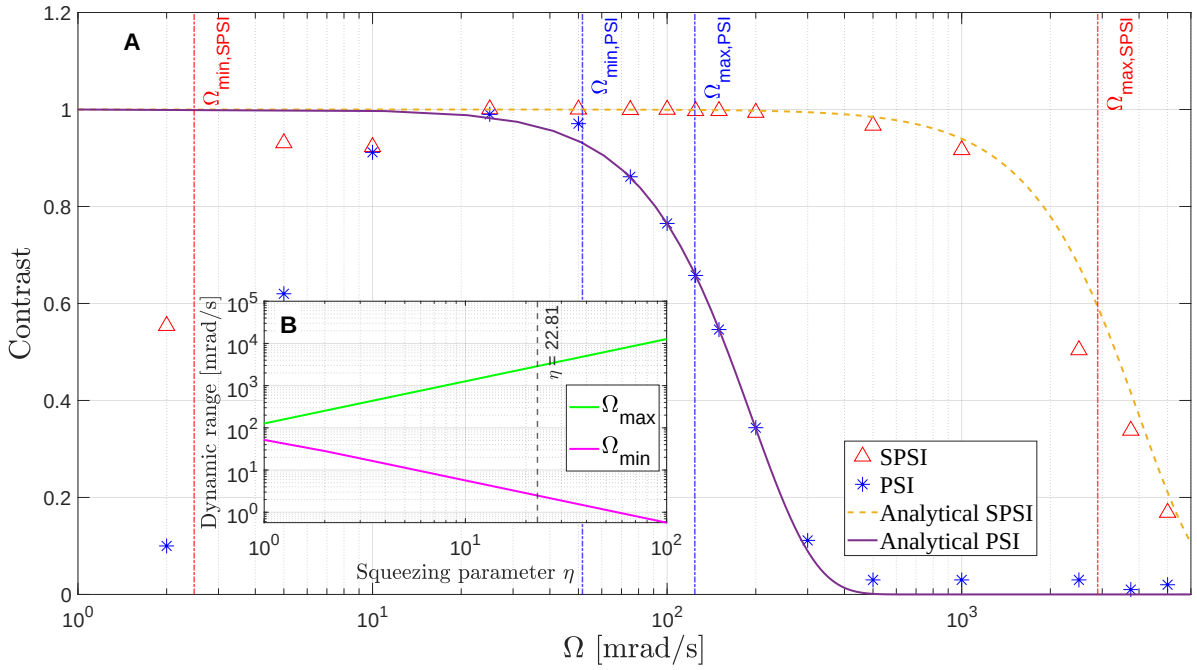

Figure 31: Contrast and dynamic range: (A) Contrast vs. angular velocity (Ω). Using ^{87}Rb atoms, the simulation parameters are initial cloud size $\sigma_{x0} = 100\,\mu$m, temperature $\mathcal{T} = 5\,\mu$K, and time between pulses $T_R = 5\,$ms. For the repulsive potential, we take a beam power of $P = 1\,$W with a cross-section of $400 \times 400\,\mu$m^2, blue-detuned by $\Delta = 2\pi \cdot 10\,$GHz, and focused such that in the direction of acceleration it gives rise to an inverted harmonic potential and in the transverse direction a constant potential. The harmonic profile was optimized to achieve a large squeezing factor before the atoms exceed the region where the repulsive potential is harmonic. Following Eqs. 60 and 63, and choosing $t_{\rm acc} = 80.6\,\mu$s, we find a squeezing parameter of 22.81. The purple line represents the analytical solution of PSI contrast, while the dashed orange line corresponds to SPSI, according to Eq. 33. The data points are the result of a numerical simulation. While the contrast reduction due to the ratio between the fringe periodicity and the initial cloud size determines the upper limit of the detection range, there exists a lower limit when the fringe period becomes larger than the final cloud size. These limits are roughly given by $\Omega_{\rm min}$ and $\Omega_{\rm max}$ (Eq. 35), which are presented in the graph as vertical dashed lines. It is evident that using the SPSI greatly improves the contrast, thereby increasing the detection dynamic range. At high angular velocities, the contrast of the data points decreases faster than the analytical solution due to the short spacing between fringes relative to the detection pixel size considered only in the numerical calculation. (B) The analytical curve of the detection range as a function of η according to Eq. 35. The dashed line presents the SPSI simulated in (A) with $\eta = 22.81$.

strates an improvement of over one order of magnitude when both methods operate within their dynamic range ($60 \lesssim \Omega \lesssim 200\,$mrad/s), with a notably superior ratio beyond that range. The plot of angular velocity deviation $\Delta\Omega = (\Omega_{\rm meas} - \Omega)$ in Fig. 32(B) further supports these findings.

5.3.2 Compactness

To demonstrate the advantage of the SPSI in terms of compactness, we introduce the dimensionless parameter $a_t = T_{R,\rm SPSI}/T_{R,\rm PSI}$, representing the reduction in Ramsey time in a compact SPSI relative

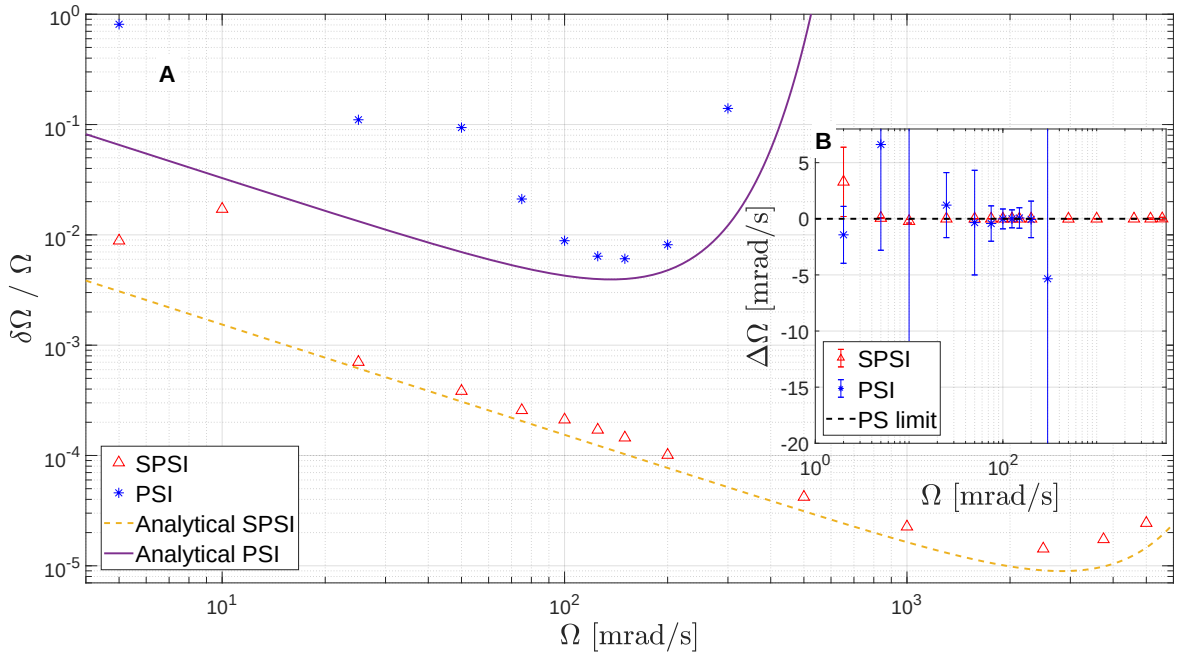

Figure 32: Relative sensitivity and measured angular velocity deviation: (A) Relative sensitivity $\delta\Omega/\Omega$ vs Ω, where Ω is the nominal (actual) angular velocity, for the same simulation parameters and notation as in Fig. 31. The analytical curves are determined according to Eq. 34. The data points for PSI are not shown at large angular velocities, since $\delta\Omega/\Omega$ exceeds the value of 1, thus irrelevant. (B) Simulation results of the measured angular velocity deviation $\Delta\Omega \equiv (\Omega_{\text{meas}} - \Omega)$ for different angular velocities. Here $\Delta\Omega$ denotes the discrepancy between the measured and nominal angular velocities, while the sensitivity (uncertainty) $\delta\Omega$ is represented by the error bars. The data point labels are the same as in (A), while the black dashed line illustrates the point-source (PS) limit of zero deviation. The data points for PSI are not shown at large angular velocities, since $\Delta\Omega$ is too large. The enhanced performance of the SPSI in dynamic range and sensitivity (measurement uncertainty) is clearly visible.

to a standard PSI ($a_t < 1$). This reduction also decreases the fall distance h during the interferometer by a_t^2. Additionally, the final cloud's radius scales as $\sigma_f \sim a_t T_{\text{ex}} \sigma_{v0} \eta$. Based on these considerations, we can express the sensitivity per shot for SPSI as:

$$\delta\Omega \sim \frac{1}{a_t T_R^2 \cdot 2k_{\text{eff}} C \sqrt{N/2} \cdot a_t \sigma_{v0} \eta}, \tag{69}$$

leading to a sensitivity per shot ratio of $\delta\Omega_{\text{SPSI}}/\delta\Omega_{\text{PSI}} = (C_{\text{PSI}}/C_{\text{SPSI}})/(a_t^2 \cdot \eta)$. While the ratios of the detection limits of PSI and SPSI are determined by:

$$\frac{\Omega_{\text{min,SPSI}}}{\Omega_{\text{min,PSI}}} = \frac{1}{a_t^2 \cdot \eta}, \quad \frac{\Omega_{\text{max,SPSI}}}{\Omega_{\text{max,PSI}}} = \frac{\eta}{a_t}. \tag{70}$$

Overall, the ratio $\Omega_{\text{max}}/\Omega_{\text{min}}$ changes by a factor of $\eta^2 \cdot a_t$.

For the design of a rotation sensor, it would be necessary to compromise between sensitivity and compactness and to identify the optimal operational point based on the parameters η and a_t. Fig. 33 illustrates the advantage in single-shot sensitivity offered by the SPSI over the standard PSI for different parameter values. It is evident that the incorporation of a repulsive potential allows for a sensitivity

enhancement of up to two orders of magnitude, while concurrently reducing the cycle time by a factor of approximately two, or alternatively, decreasing the cycle time by around tenfold without compromising sensitivity.

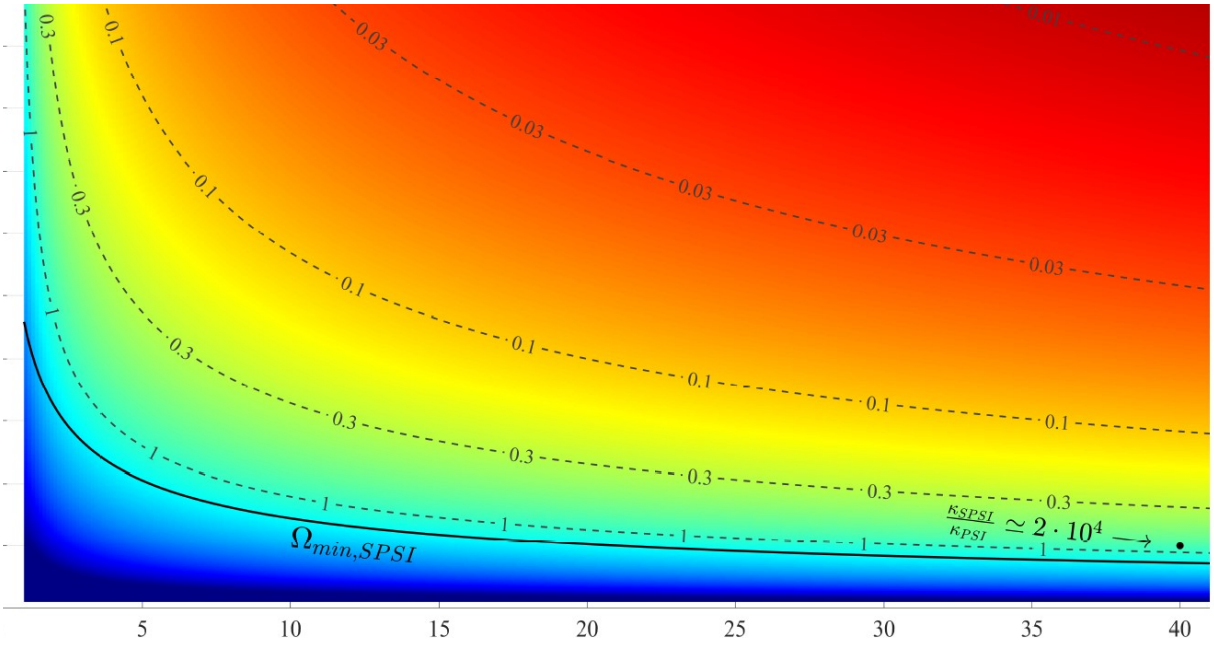

Figure 33: Sensitivity-compactness trade-off in the SPSI: The plot shows the single-shot sensitivity ratio $\delta\Omega_{SPSI}/\delta\Omega_{PSI}$ (Eq. 69) as a function of the squeezing parameter η and the cycle time ratio $a_t = T_{SPSI}/T_{PSI}$. The simulation parameters are: angular velocity $\Omega = 100\,\text{mrad/s}$, Ramsey time $T_R = 10\,\text{ms}$, temperature $\mathcal{T} = 2\,\mu\text{K}$, and initial cloud size $\sigma_{x0} = 100\,\mu\text{m}$. The maximum value of η ensures most atoms experience the same potential during acceleration. The bold black line indicates the validity boundary of this plot, beyond which the minimal detectable angular velocity of the SPSI method (Eq. 70) exceeds the nominal angular velocity Ω. It is evident that the implementation of a repulsive potential allows for a sensitivity enhancement of more than an order of magnitude while simultaneously reducing the cycle time by a factor of about two (indicated in bright red) or reducing the cycle time by approximately tenfold without affecting the sensitivity (indicated in light-blue). Specifically, utilizing the compactness factor definition of Eq. 71, we find that with $\eta = 40$ and $a_t = 0.1$, we have a performance enhancement of $CF_{SPSI}/CF_{PSI} \simeq 2 \cdot 10^4$ (black point).

Considering that sensitivity per unit time (Eq. 34 scales as the inverse square root of the repetition rate $\nu = 1/\tau_{\text{rep}}$, and noting that the repetition rate ratio between SPSI and standard PSI scales as a_t, we derive the sensitivity ratio per unit time as $\delta\Omega_{SPSI}/\delta\Omega_{PSI} = (C_{PSI}/C_{SPSI})/a_t^{1.5} \cdot \eta$.

To better quantify the performance improvement, we introduce a compactness factor:

$$CF \equiv \frac{\Omega_{\text{max}}/\Omega_{\text{min}}}{\delta\Omega \cdot h}. \tag{71}$$

This factor encapsulates sensitivity $\delta\Omega$ (Eq. 69), dynamic range (as the ratio $\Omega_{\text{max}}/\Omega_{\text{min}}$, Eq. 70), and the vertical size of the interferometer h. Based on the previous comparison between SPSI and PSI, we observe an improvement ratio of $\eta^3 \cdot \sqrt{a_t}$, which can exceed four orders of magnitude. For instance, considering the conditions depicted in Fig. 33, with $\eta = 40$ and $a_t = 0.1$, we derive $CF_{\text{SPSI}}/CF_{\text{PSI}} \simeq 2{\cdot}10^4$.

5.3.3 Chip-Scale Device Potential

To explore the potential for miniaturization, we compare standard PSI and SPSI under constraints relevant to chip-scale devices. Let us now compare standard PSI with SPSI within the constraints of identical Ramsey times ($a_t = 1$) and fall heights h in the context of chip-scale devices. Employing the repulsive potential to expand acceleration parallel to the chip's plane enables the SPSI method to optimize the device's confinement.

For the comparison, under the same initial conditions (temperature, cloud size, and number of atoms), the ratio between the sensitivities obtained in the two methods is $\delta\Omega_{\mathrm{SPSI}}/\delta\Omega_{\mathrm{PSI}} \approx (C_{\mathrm{PSI}}/C_{\mathrm{SPSI}})/\eta$. Within the dynamic range of both methods, the contrast ratio is approximately unity, while the detection limits ratio is the same as in Sec. 5.3.1. Consequently, for chip-scale devices, we can expect the sensitivity improvement of about η and an increase in the dynamic range $\Omega_{\max}/\Omega_{\min}$ by a factor of η^2.

For a future chip-scale device, we consider a scenario with a rectangular vacuum cell of dimensions $1\,\mathrm{mm} \times 10\,\mathrm{mm} \times 10\,\mathrm{mm}$, with the short dimension aligned perpendicular to the direction of the repulsive potential's acceleration. Using realistic parameters ($N = 10^6$ ^{87}Rb atoms, $\sigma_{x0} = 100\,\mu\mathrm{m}$, $\mathcal{T} = 2\,\mu\mathrm{K}$, $T_R = 2.5\,\mathrm{ms}$), and employing a fully harmonic potential characterized by dimensions of $x_0 = 200\,\mu\mathrm{m}$ and $z_0 = 400\,\mu\mathrm{m}$, with total power of $P = 1\,\mathrm{W}$ and an acceleration time of $t_{\mathrm{acc}} = 0.1\,\mathrm{ms}$, we achieve a squeezing parameter $\eta = 46.2$ and a final velocity uncertainty $\tilde{\sigma}v0 = 0.64\,\mathrm{m/s}$. The final cloud dimensions are $\sigma_{f,z} = 170\,\mu\mathrm{m}$ height and $\sigma_{f,x} = 0.33\,\mathrm{cm}$ width. Without heating (Sec. 5.1.2), a vacuum dimension of 0.5 mm would suffice, but if heating is not mitigated, a vacuum dimension of 1 mm would be required, or alternatively, one would have to take into account that a considerable number of atoms could not be recaptured for the next cycle, and reloading atoms from a source would be required.

With an operation rate of $\tau = 100\,\mathrm{s}^{-1}$, the SPSI exhibits a sensitivity of $\delta\Omega = 1\,\mu\mathrm{rad}/(\mathrm{s}\cdot\sqrt{\mathrm{Hz}})$ and a one-shot sensitivity of $\delta\Omega = 10\,\mu\mathrm{rad/s}$. The minimum and maximum detectable angular velocities are $\Omega\mathrm{min} = 7.5\,\mathrm{mrad/s}$ and $\Omega_{\max} = 11.47\,\mathrm{rad/s}$, respectively. These results demonstrate that SPSI can achieve high sensitivity and a wide dynamic range within the constraints of a chip-scale device, offering a ~ 46-fold improvement in sensitivity and more than 3 orders of magnitude increase in dynamic range compared to standard PSI under the same conditions.

In conclusion, our performance analysis demonstrates that the SPSI method offers significant advantages over conventional PSI techniques in terms of sensitivity, dynamic range, and potential for miniaturization. These improvements pave the way for the development of high-performance, compact rotation sensors with applications in inertial navigation, geophysics, and fundamental physics experiments.

References

1. Kasevich, M. & Chu, S. Atomic interferometry using stimulated Raman transitions. en. *Phys. Rev. Lett.* **67,** 181–184 (July 1991).
2. Keith, D. W., Ekstrom, C. R., Turchette, Q. A. & Pritchard, D. E. An interferometer for atoms. en. *Phys. Rev. Lett.* **66,** 2693–2696 (May 1991).
3. Carnal, O. & Mlynek, J. Young's double-slit experiment with atoms: A simple atom interferometer. en. *Phys. Rev. Lett.* **66,** 2689–2692 (May 1991).
4. Riehle, F., Kisters, T., Witte, A., Helmcke, J. & Bordé, C. J. Optical Ramsey spectroscopy in a rotating frame: Sagnac effect in a matter-wave interferometer. en. *Phys. Rev. Lett.* **67,** 177–180 (July 1991).
5. Robert, J. *et al.* Atomic Interferometry with Metastable Hydrogen Atoms. *Europhys. Lett.* **16,** 29–34 (Sept. 1991).
6. Cronin, A. D., Schmiedmayer, J. & Pritchard, D. E. Optics and interferometry with atoms and molecules. en. *Rev. Mod. Phys.* **81,** 1051–1129 (July 2009).
7. Barrett, B. *et al.* The Sagnac effect: 20 years of development in matter-wave interferometry. en. *Comptes Rendus Physique* **15,** 875–883 (Dec. 2014).
8. Barrett, B., Bertoldi, A. & Bouyer, P. Inertial quantum sensors using light and matter. *Phys. Scr.* **91,** 053006 (May 2016).
9. McGuinness, H. J., Rakholia, A. V. & Biedermann, G. W. High data-rate atom interferometer for measuring acceleration. en. *Applied Physics Letters* **100,** 011106 (Jan. 2012).
10. Battelier, B. *et al. Development of compact cold-atom sensors for inertial navigation* in (eds Stuhler, J. & Shields, A. J.) (Brussels, Belgium, Apr. 2016), 990004.
11. Gillot, P., Francis, O., Landragin, A., Pereira Dos Santos, F. & Merlet, S. Stability comparison of two absolute gravimeters: optical versus atomic interferometers. *Metrologia* **51,** L15–L17 (Oct. 2014).
12. Bertoldi, A. *et al.* AEDGE: Atomic experiment for dark matter and gravity exploration in space. en. *Exp Astron* **51,** 1417–1426 (June 2021).
13. Bassi, A. *et al.* A way forward for fundamental physics in space. en. *npj Microgravity* **8,** 49 (Nov. 2022).
14. Elliott, E. R. *et al.* Quantum gas mixtures and dual-species atom interferometry in space. en. *Nature* **623,** 502–508 (Nov. 2023).
15. Abend, S. *et al.* Technology roadmap for cold-atoms based quantum inertial sensor in space. en. *AVS Quantum Science* **5,** 019201 (Mar. 2023).
16. Gustavson, T. L., Landragin, A. & Kasevich, M. A. Rotation sensing with a dual atom-interferometer Sagnac gyroscope. *Class. Quantum Grav.* **17,** 2385–2398 (June 2000).
17. Durfee, D. S., Shaham, Y. K. & Kasevich, M. A. Long-Term Stability of an Area-Reversible Atom-Interferometer Sagnac Gyroscope. en. *Phys. Rev. Lett.* **97,** 240801 (Dec. 2006).
18. Canuel, B. *et al.* Six-Axis Inertial Sensor Using Cold-Atom Interferometry. en. *Phys. Rev. Lett.* **97,** 010402 (July 2006).

19. Gauguet, A., Canuel, B., Lévèque, T., Chaibi, W. & Landragin, A. Characterization and limits of a cold-atom Sagnac interferometer. en. *Phys. Rev. A* **80,** 063604 (Dec. 2009).

20. Stevenson, R., Hush, M. R., Bishop, T., Lesanovsky, I. & Fernholz, T. Sagnac Interferometry with a Single Atomic Clock. en. *Phys. Rev. Lett.* **115,** 163001 (Oct. 2015).

21. Gautier, R. *et al.* Accurate measurement of the Sagnac effect for matter waves. *Science Advances* **8,** eabn8009 (June 2022).

22. Janvier, C. *et al.* Compact differential gravimeter at the quantum projection-noise limit. en. *Phys. Rev. A* **105,** 022801 (Feb. 2022).

23. Savoie, D. *et al.* Interleaved atom interferometry for high-sensitivity inertial measurements. en. *Sci. Adv.* **4,** eaau7948 (Dec. 2018).

24. Geiger, R. *et al. Continuous cold atom inertial sensor with 1 nrad.s^-1 rotation stability(Conference Presentation)* in *Quantum Optics* (eds Shields, A. J. & Stuhler, J.) (SPIE, Brussels, Belgium, Aug. 2016), 4.

25. McGuirk, J. M., Snadden, M. J. & Kasevich, M. A. Large Area Light-Pulse Atom Interferometry. *Phys. Rev. Lett.* **85,** 4498–4501 (Nov. 2000).

26. Chiow, S.-w., Kovachy, T., Chien, H.-C. & Kasevich, M. A. 102 $\hbar$ k Large Area Atom Interferometers. en. *Phys. Rev. Lett.* **107,** 130403 (Sept. 2011).

27. Kovachy, T. *et al.* Quantum superposition at the half-metre scale. en. *Nature* **528,** 530–533 (Dec. 2015).

28. Plotkin-Swing, B. *et al.* Three-Path Atom Interferometry with Large Momentum Separation. en. *Phys. Rev. Lett.* **121,** 133201 (Sept. 2018).

29. Rudolph, J. *et al.* Large Momentum Transfer Clock Atom Interferometry on the 689 nm Intercombination Line of Strontium. *Phys. Rev. Lett.* **124,** 083604 (Feb. 2020).

30. Parker, R. H., Yu, C., Zhong, W., Estey, B. & Müller, H. Measurement of the fine-structure constant as a test of the Standard Model. en. *Science* **360,** 191–195 (Apr. 2018).

31. Gebbe, M. *et al.* Twin-lattice atom interferometry. en. *Nat. Commun.* **12,** 2544 (May 2021).

32. Li, J. *et al.* High Sensitivity Multi-Axes Rotation Sensing Using Large Momentum Transfer Point Source Atom Interferometry. en. *Atoms* **9,** 51 (Aug. 2021).

33. Dubetsky, B. Sequential large momentum transfer exploiting rectangular Raman pulses. en. *Phys. Rev. A* **108,** 063308 (Dec. 2023).

34. Siemß, J.-N. *et al.* Large-momentum-transfer atom interferometers with μrad-accuracy using Bragg diffraction. en. *Phys. Rev. Lett.* **131,** 033602 (July 2023).

35. Goerz, M. H., Kasevich, M. A. & Malinovsky, V. S. Robust Optimized Pulse Schemes for Atomic Fountain Interferometry. en. *Atoms* **11,** 36 (Feb. 2023).

36. Li, J. *et al.* Spin-squeezing-enhanced dual-species atom interferometric accelerometer employing large momentum transfer for precision test of the equivalence principle. en. *Phys. Rev. D* **108,** 024011 (July 2023).

37. Louie, G., Chen, Z., Deshpande, T. & Kovachy, T. Robust atom optics for Bragg atom interferometry. *New J. Phys.* **25,** 083017 (Aug. 2023).

38. Hosten, O., Engelsen, N. J., Krishnakumar, R. & Kasevich, M. A. Measurement noise 100 times lower than the quantum-projection limit using entangled atoms. *Nature* **529,** 505–508 (Jan. 2016).

39. Salvi, L., Poli, N., Vuletic, V. & Tino, G. M. Squeezing on Momentum States for Atom Interferometry. *Phys. Rev. Lett.* **120.** Publisher: American Physical Society, 033601 (Jan. 2018).

40. Geiger, R. *et al.* Detecting inertial effects with airborne matter-wave interferometry. *Nature Communications* **2,** 474 (Sept. 2011).

41. Ménoret, V. *et al.* Dual-wavelength laser source for onboard atom interferometry. *Opt. Lett.* **36.** Publisher: Optica Publishing Group, 4128–4130 (Nov. 2011).

42. Bidel, Y. *et al.* Compact cold atom gravimeter for field applications. en. *Applied Physics Letters* **102,** 144107 (Apr. 2013).

43. Dickerson, S. M., Hogan, J. M., Sugarbaker, A., Johnson, D. M. S. & Kasevich, M. A. Multiaxis Inertial Sensing with Long-Time Point Source Atom Interferometry. en. *Phys. Rev. Lett.* **111,** 083001 (Aug. 2013).

44. Givon, M. *Walks on the Bloch sphere: Coherent manipulations of an atomic two-state system* en. 2006.

45. Stefan Kuhr. *A controlled quantum system of individual neutral atoms* PhD thesis (Rheinische Friedrich-Wilhelms-Universität Bonn, 2003).

46. Givon, M. *A Magic Frequency in Light-Matter Interaction of a Two-State System with Multiple Degeneracy* en. PHD (Ben-Gurion University, Beer Sheva, Israel, Nov. 2014).

47. Shore, B. *The Theory of Coherent Atomic Excitation* en (Jhon Wiley & Sons, New York, May 1991).

48. Avinadav, C. *Improving the dynamic range and stability of acceleration and rotation sensing atom interferometers* en. PHD (Weizmann Institute of Science, Rehovot, Israel, Nov. 2020).

49. Yankelev, D. *Atom interferometry with improved sensitivity, stability and dynamic range* en. PHD (Weizmann Institute of Science, Rehovot, Israel, July 2020).

50. Sagnac, G. Effet tourbillonnaire optique. La circulation de l'éther lumineux dans un interférographe tournant. *J. Phys. Theor. Appl.* **4,** 177–195 (1914).

51. Chen, Y.-J. *et al.* Single-Source Multiaxis Cold-Atom Interferometer in a Centimeter-Scale Cell. en. *Phys. Rev. Applied* **12,** 014019 (July 2019).

52. Avinadav, C., Yankelev, D., Shuker, M., Firstenberg, O. & Davidson, N. Rotation sensing with improved stability using point-source atom interferometry. en. *Phys. Rev. A* **102,** 013326 (July 2020).

53. Hoth, G. W., Pelle, B., Riedl, S., Kitching, J. & Donley, E. A. Point source atom interferometry with a cloud of finite size. en. *Appl. Phys. Lett.* **109,** 071113 (Aug. 2016).

54. Hoth, G. W., Pelle, B., Kitching, J. & Donley, E. A. *Analytical tools for point source interferometry* en. in *Slow Light, Fast Light, and Opto-Atomic Precision Metrology X* (eds Shahriar, S. M. & Scheuer, J.) **10119** (SPIE, Feb. 2017), 1011908.

55. Gauguet, A. *et al.* Off-resonant Raman transition impact in an atom interferometer. en. *Phys. Rev. A* **78,** 043615 (Oct. 2008).

56. Stockton, J. K., Takase, K. & Kasevich, M. A. Absolute Geodetic Rotation Measurement Using Atom Interferometry. en. *Phys. Rev. Lett.* **107,** 133001 (Sept. 2011).

57. Berg, P. *et al.* Composite-Light-Pulse Technique for High-Precision Atom Interferometry. en. *Phys. Rev. Lett.* **114,** 063002 (Feb. 2015).

58. Yao, Z.-W. *et al.* Calibration of atomic trajectories in a large-area dual-atom-interferometer gyroscope. en. *Phys. Rev. A* **97,** 013620 (Jan. 2018).

59. Li, J., Kovachy, T., Bonacum, J. & Shahriar, S. M. *Sensitivity analysis of point source interferometers augmented with large momentum transfer* in *Quantum Sensing, Imaging, and Precision Metrology II* (eds Shahriar, S. M. & Scheuer, J.) (SPIE, Mar. 2024), 76.

60. Foster, G. T., Fixler, J. B., McGuirk, J. M. & Kasevich, M. A. Method of phase extraction between coupled atom interferometers using ellipse-specific fitting. en. *Opt. Lett.* **27,** 951 (June 2002).

61. Sugarbaker, A., Dickerson, S. M., Hogan, J. M., Johnson, D. M. S. & Kasevich, M. A. Enhanced Atom Interferometer Readout through the Application of Phase Shear. en. *Phys. Rev. Lett.* **111,** 113002 (Sept. 2013).

62. Chen, Y.-J. *et al.* Robust inertial sensing with point-source atom interferometry for interferograms spanning a partial period. en. *Opt. Express* **28,** 34516 (Nov. 2020).

63. Castin, Y. & Dum, R. Bose-Einstein Condensates in Time Dependent Traps. en. *Phys. Rev. Lett.* **77,** 5315–5319 (Dec. 1996).

64. Japha, Y. Unified model of matter-wave-packet evolution and application to spatial coherence of atom interferometers. en. *Phys. Rev. A* **104,** 053310 (Nov. 2021).

65. Miller, D. E. *et al.* High-contrast interference in a thermal cloud of atoms. en. *Phys. Rev. A* **71,** 043615 (Apr. 2005).

66. Cheinet, P. *et al.* Measurement of the Sensitivity Function in a Time-Domain Atomic Interferometer. en. *IEEE Trans. Instrum. Meas.* **57,** 1141–1148 (June 2008).

67. Dick, G. J. *Local Oscillator Induced Instabilities in Trapped Ion Frequency Standards* in *Proceedings of the 19th Annual Precise Time and Time Interval Systems and Applications Meeting* (Dec. 1987), 133–147.

68. Gouët, J. L. *et al.* Limits to the sensitivity of a low noise compact atomic gravimeter. en. *Appl. Phys. B* **92,** 133–144 (Aug. 2008).

69. Nyman, R. *et al.* I.C.E.: a transportable atomic inertial sensor for test in microgravity. *Applied Physics B* **84,** 673–681 (Sept. 2006).

70. Freier, C. *Measurement of Local Gravity using Atom Interferometry* en. PHD (Humboldt-University, Berlin, Germany, Aug. 2010).

71. Riedl, S., Hoth, G. W., Pelle, B., Kitching, J. & Donley, E. A. Compact atom-interferometer gyroscope based on an expanding ball of atoms. en. *J. Phys.: Conf. Ser.* **723,** 012058 (June 2016).

72. Wang, K. *et al.* Hybrid wide-band, low-phase-noise scheme for Raman lasers in atom interferometry by integrating an acousto-optic modulator and a feedback loop. *Appl. Opt.* **55.** Publisher: Optica Publishing Group, 989–992 (Feb. 2016).

73. Peters, A., Chung, K. Y. & Chu, S. High-precision gravity measurements using atom interferometry. *Metrologia* **38,** 25–61 (Feb. 2001).

74. Grimm, R., Weidemüller, M. & Ovchinnikov, Y. B. en. in *Advances In Atomic, Molecular, and Optical Physics* 95–170 (Elsevier, 2000).

75. Amit, O. *Non-Perturbing Probing of the 87Rb Clock Transition* MSc (Ben-Gurion University of the Negev, Beer Sheva, Israel, Apr. 2015).

76. Chaudhuri, S., Roy, S. & Unnikrishnan, C. S. Realization of an intense cold Rb atomic beam based on a two-dimensional magneto-optical trap: Experiments and comparison with simulations. en. *Phys. Rev. A* **74,** 023406 (Aug. 2006).

77. Steck, D. A. *Rubidium 87 D Line rev2.2.2.pdf* tech. rep. (University of Oregon, Eugene, Oregon, July 2021).

78. Lan, S.-Y., Kuan, P.-C., Estey, B., Haslinger, P. & Müller, H. Influence of the Coriolis Force in Atom Interferometry. en. *Phys. Rev. Lett.* **108,** 090402 (Feb. 2012).

79. Zhao, Y., Yue, X., Chen, F. & Huang, C. Extension of the rotation-rate measurement range with no sensitivity loss in a cold-atom gyroscope. en. *Phys. Rev. A* **104,** 013312 (July 2021).

80. Lin, Y.-J., Perry, A. R., Compton, R. L., Spielman, I. B. & Porto, J. V. Rapid production of R 87 b Bose-Einstein condensates in a combined magnetic and optical potential. en. *Phys. Rev. A* **79,** 063631 (June 2009).

81. Krzyzanowska, K. A., Ferreras, J., Ryu, C., Samson, E. C. & Boshier, M. G. Matter-wave analog of a fiber-optic gyroscope. *Phys. Rev. A* **108,** 043305 (Oct. 2023).

82. Jia, W., Yan, P., Wang, S. & Feng, Y. A Dual Atomic Interferometric Inertial Sensor Utilizing Transversely Cooled Atomic Beams. *2024 IEEE International Symposium on Inertial Sensors and Systems (INERTIAL),* 1–4 (2024).

83. Ammann, H. & Christensen, N. Delta Kick Cooling: A New Method for Cooling Atoms. en. *Phys. Rev. Lett.* **78,** 2088–2091 (Mar. 1997).

84. Kovachy, T. *et al.* Matter Wave Lensing to Picokelvin Temperatures. en. *Phys. Rev. Lett.* **114,** 143004 (Apr. 2015).

85. Luan, T., Li, Y., Zhang, X. & Chen, X. Realization of two-stage crossed beam cooling and the comparison with Delta-kick cooling in experiment. en. *Review of Scientific Instruments* **89,** 123110 (Dec. 2018).

86. Dupays, L., Spierings, D. C., Steinberg, A. M. & Del Campo, A. Delta-kick cooling, time-optimal control of scale-invariant dynamics, and shortcuts to adiabaticity assisted by kicks. en. *Phys. Rev. Research* **3,** 033261 (Sept. 2021).

87. Pandey, S., Mas, H., Vasilakis, G. & Von Klitzing, W. Atomtronic Matter-Wave Lensing. en. *Phys. Rev. Lett.* **126,** 170402 (Apr. 2021).

88. Romero-Isart, O. Coherent inflation for large quantum superpositions of levitated microspheres. *New J. Phys.* **19,** 123029 (Dec. 2017).

89. Yuce, C. Quantum inverted harmonic potential. *Phys. Scr.* **96,** 105006 (Oct. 2021).

90. Weiss, T., Roda-Llordes, M., Torrontegui, E., Aspelmeyer, M. & Romero-Isart, O. Large Quantum Delocalization of a Levitated Nanoparticle Using Optimal Control: Applications for Force Sensing and Entangling via Weak Forces. en. *Phys. Rev. Lett.* **127,** 023601 (July 2021).

91. Ullinger, F., Zimmermann, M. & Schleich, W. P. The logarithmic phase singularity in the inverted harmonic oscillator. en. *AVS Quantum Science* **4,** 024402 (June 2022).

92. Neumeier, L., Ciampini, M. A., Romero-Isart, O., Aspelmeyer, M. & Kiesel, N. Fast quantum interference of a nanoparticle via optical potential control. en. *Proc. Natl. Acad. Sci. U.S.A.* **121** (Jan. 2024).

93. Rozenman, G. G. *et al.* Observation of a phase space horizon with surface gravity water waves. en. *Commun Phys* **7,** 165 (May 2024).

אינטרפרומטרה אטומית לחישת סיבוב

ילי סינה

תואר מוסמך במדעים

אוניברסיטת בן-גוריון בנגב

תשפ"ה

תקציר

תזה זו מציגה את הפיתוח של אינטרפרומטר אטומי בעל מקור נקודתי (PSI) למדידת סיבוב בדיוק גבוה. אנו מציגים התקדמויות ניסיוניות ותיאורטיות בטכנולוגיית PSI תוך התמקדות בשיפור הרגישות, הטווח הדינמי, והפוטנציאל למיניאטוריזציה.

העבודה הניסיונית שלנו כוללת תכנון ובנייה של מערכת דו-תאית רב-תכליתית, הכוללת מלכודת מגנטו-אופטית דו-ממדית (2D-MOT) ליצירת אטומים קרים, ותא מלכודת מגנטו-אופטית תלת-ממדית (3D-MOT) ללכידת אטומים ואינטרפרומטריה. אלמנט מרכזי הוא שילוב סלילים מגנטיים בעלי גרדיאנט גבוהה בתוך תא הוואקום, המאפשר כליאת אטומים חזקה תוך מזעור צריכת החשמל ויצירת החום.

בחזית התיאורטית, אנו מציגים את שיטת האינטרפרומטר האטומי של מקור נקודתי דחוס (SPSI) המשלבת פוטנציאל דוחה כדי לתמרן את התפלגות מרחב הפאזה של מכלול האטומים לפני תהליך האינטרפרומטר. באמצעות פיתוח אנליטי וסימולציות נומריות, אנו מדגימים כי SPSI יכול לשפר את רגישות האינטרפרומטר עד פי מאה תוך הפחתת זמן המחזור בו-זמנית.

אנו מציגים ניתוח ביצועים מקיף, ומגדירים את פקטור הקומפקטיות המשלב את מידת הרגישות, הטווח הדינמי, ומימדי המכשיר. התוצאות מראות שיפור של עד פי עשרת אלפים לעומת תצורות PSI סטנדרטיות, וסוללות את הדרך לפיתוח אינטרפרומטרים אטומיים בקנה מידה של שבב למדידת סיבוב.

עבודה זו תורמת לקידום טכנולוגיית האינטרפרומטריה האטומית ומרחיבה את יכולות המדידה המדויקת, תוך התקדמות משמעותית לקראת מכשירים קומפקטיים ליישומים בעולם האמיתי בניווט אינרציאלי, גיאופיזיקה, ובדיקות פיזיקה בסיסית.

אוניברסיטת בן-גוריון בנגב
הפקולטה למדעי הטבע
המחלקה לפיזיקה

אינטרפרומטרה אטומית לחישת סיבוב

חיבור זה מהווה חלק מהדרישות לקבלת התואר מוסמך
למדעי הטבע (M.Sc)

על ידי

ילי סינה

העבודה נכתבה בהנחייתו של

פרופ' רון פולמן

חשוון תשפ"ה